

Accepted Manuscript

Novel EGCG assisted ultrasound synthesis of self-assembled Ca_2SiO_4 : Eu^{3+} hierarchical superstructures: Photometric characteristics and LED applications

M. Venkataravanappa, H. Nagabhushana, G.P. Darshan, B. Daruka Prasad, G.R. Vijayakumar, H.B. Premkumar, Udayabhanu

PII: S1350-4177(16)30094-3

DOI: <http://dx.doi.org/10.1016/j.ultsonch.2016.03.028>

Reference: ULTSON 3170

To appear in: *Ultrasonics Sonochemistry*

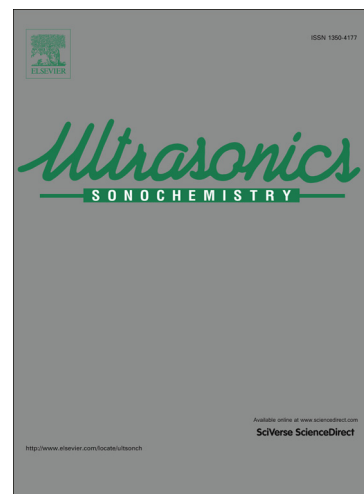
Received Date: 6 March 2016

Revised Date: 27 March 2016

Accepted Date: 30 March 2016

Please cite this article as: M. Venkataravanappa, H. Nagabhushana, G.P. Darshan, B. Daruka Prasad, G.R. Vijayakumar, H.B. Premkumar, Udayabhanu, Novel EGCG assisted ultrasound synthesis of self-assembled Ca_2SiO_4 : Eu^{3+} hierarchical superstructures: Photometric characteristics and LED applications, *Ultrasonics Sonochemistry* (2016), doi: <http://dx.doi.org/10.1016/j.ultsonch.2016.03.028>

This is a PDF file of an unedited manuscript that has been accepted for publication. As a service to our customers we are providing this early version of the manuscript. The manuscript will undergo copyediting, typesetting, and review of the resulting proof before it is published in its final form. Please note that during the production process errors may be discovered which could affect the content, and all legal disclaimers that apply to the journal pertain.



Novel EGCG assisted ultrasound synthesis of self-assembled $\text{Ca}_2\text{SiO}_4:\text{Eu}^{3+}$ hierarchical superstructures: Photometric characteristics and LED applications

M. Venkataravanappa^{1,2}, H. Nagabhushana^{3*}, G.P. Darshan^{4,2}, B. Daruka Prasad⁵,
G.R. Vijayakumar⁶, H. B Premkumar⁷, Udayabhanu⁸

¹Department of Physics, Govt. First Grade College, Sira, Tumkur 572 103, India

²Research and Development Center, Bharathiar University, Coimbatore 641046, India

³Prof. C.N.R. Rao Centre for Advanced Materials, Tumkur University, Tumkur 572 103, India

⁴Department of Physics, Acharya Institute of Graduate Studies, Bangalore 560 107, India

⁵Department of Physics, BMS Institute of Technology, VTU-affiliated, Bangalore 560 064, India

⁶Department of Chemistry, University College of Science, Tumkur University, Tumkur 572103, India

⁷Department of Physics, Dayananda Sagar Academy of Technology and Management, Bangalore 560082, India

⁸Department of Chemistry, Siddaganga Institute of Technology, Tumkur 572103, India

Abstract

This paper reports for the first time ultrasound, EGCG assisted synthesis of pure and Eu^{3+} (1-5 mol %) activated Ca_2SiO_4 nanophosphors having self-assembled superstructures with high purity. The shape, size and morphology of the product were tuned by controlling influential parameters. It was found that morphology was highly dependent on EGCG concentration, sonication time, pH and sonication power. The probable formation mechanism for various hierarchical superstructures was proposed. The PL studies of $\text{Ca}_2\text{SiO}_4:\text{Eu}^{3+}$ phosphors can be effectively excited by the near ultraviolet (UV) (396 nm) light and exhibited strong red emission around 613 nm, which was attributed to the Eu^{3+} (${}^5\text{D}_0 \rightarrow {}^7\text{F}_2$) transition. The concentration quenching phenomenon was explained based on defect to Eu^{3+} energy transfer, electron-phonon coupling and Eu^{3+} - Eu^{3+} interaction. The Judd–Ofelt intensity parameters and radiative properties were estimated by using PL emission spectra. The photometric studies indicate that the obtained phosphors could be a promising red component for possible applications in the field of white light emitting diodes.

Keywords: Sonochemical synthesis; Nanophosphor; Light emitting diodes; Photoluminescence; Superstructures.

* Corresponding author: +91- 9945954010, E-mail: bhushanvlc@gmail.com (H. Nagabhushana).

1. Introduction

Advances in nano/bulk superstructures have been led by the improvement of novel synthesis routes which offer the control of size, morphology, surface area of the product for selective applications. Recently, it has been reported that various nanostructures have been prepared by sonochemical process with several advantages over other methods namely uniform size distribution, higher surface area and high purity. In this method, consumption of high intensity ultrasound offers a novel and versatile approach for obtaining self assembled nanomaterials. The chemical reaction which occurs at high temperature and pressure in a short duration of time provides the necessary environment for the nucleation and to self oriented hierarchical superstructures [1, 2]. The molecules in the solution undergo chemical reaction followed by acoustic cavitation and formation (nucleation) of bubbles. Further, when it was subjected to ultrasonic radiation (20 kHz-10 MHz) there will be a growth by diffusion of solute atoms into the bubbles and mechanical collapse of critical – sized bubbles in the liquid solutions. During collapsing (< 1 ns), the temperature and cooling rate was extremely high (5000 - 25,000 K, $> 10^{11}$ K/s), causing the broken of chemical bonds. Further, in ultrasonic irradiation faster hydrolysis rate was achieved as a result crystallinity of material greatly enhanced [2].

Nanophosphors may have more advantages over traditional micron sized phosphors as a result, electrical and optical properties greatly enhanced. Further, nano sized particles exhibit quantum size effect, as well as high surface to volume ratio, band gap can reduce, enhance the luminescence and improves the surface and interfacial effects [3, 4]. Therefore, phosphors are significant materials for the potential applications, like fluorescent lamps, light emitting diodes (LEDs), field emission display (FEDs), plasma display panels (PDPs) and high energy detectors [5, 6]. Among these applications phosphor converted white light emitting diodes (pc-WLEDs) are important candidates for solid state lighting because of their excellent properties such as long

operational lifetime, energy saving, high brightness, higher luminescent efficiency, compactness, and environment friendliness [7].

Silicates are highly chemical resistance and visible light transparency and hence they are attractive class of inorganic materials used for wide range of applications [8]. Further, they have been extensively studied due to their high thermal, chemical stabilities, low cost, excellent water resistance and strong absorption in the near-UV region [9]. RE activated silicate phosphors have considerable practical applications such as display devices, detectors systems, immunoassays, scintillators, LEDs etc. Table.1 shows the various Eu^{3+} activated silicate hosts prepared by different chemical methods [10-16].

Herein, for the first time we report controlled fabrication of several hierarchical superstructures of $\text{Ca}_2\text{SiO}_4:\text{Eu}^{3+}$ nanophosphor with high yield and good uniformity using EGCG ultrasound assisted synthesis. In addition, various novel self-oriented superstructures were also obtained by varying the experimental conditions. Effect of morphology on sonochemical time, power and the pH of the precursor solution were discussed in detail. The possible formation mechanism of different hierarchical superstructures was put forward on the basis of time-dependent experiments. To evaluate the potential applications of the product, the photometric properties (PL, CIE, CCT and color purity) of $\text{Ca}_2\text{SiO}_4:\text{Eu}^{3+}$ nano/ micro superstructures were studied in detail.

2. Synthesis

Undoped and Eu^{3+} doped Ca_2SiO_4 nano/microstructures with varying Eu^{3+} ions concentrations were synthesized by EGCG assisted ultrasound method. The chemicals used for the synthesis were tabulated in Table 2. The stoichiometric quantities of precursors were considered for the preparation of Eu^{3+} doped Ca_2SiO_4 . 11.099 g of CaCl_2 as a source of calcium dissolved in 50 ml of distilled water and 11.18 ml of tetra ethyl orthosilicate (TEOS) as a source of silicate in to

distilled water which make up the solution to 50 ml. These aqueous solutions were thoroughly mixed in a magnetic stirrer to get a uniform solution. The different concentrations of Eu^{3+} ions (1- 5 mol %) was also added in the above solution. 5 g of EGCG ($\text{C}_{22}\text{H}_{18}\text{O}_{11}$; 458.372 g / mol) extract was dissolved in 100ml double distilled water and added to the resultant mixture slowly (5, 10, 15, 20 and 25 ml). Then, the solution mixture was stirred ultrasonically (ultrasonic frequency 20 kHz, power 300 W) at fixed temperature of 60 ± 3 °C and by varying sonication time (1 - 6 h). The solution was kept undisturbed until a white precipitate was formed. The precipitate was filtered and washed several times by distilled water and ethanol to remove any unreacted material in the centrifuge instrument. The precipitated powder was dried at 60 ± 3 °C for 3 h in a vacuum oven and calcined at 950 ± 10 °C used for further characterizations. The schematic diagram for the synthesis of Eu^{3+} doped Ca_2SiO_4 nanophosphor was shown in Fig.1.

2.1. Characterization

Phase purity and crystallinity of nanophosphors were measured using a powder X-ray diffractometer (PXRD, Shimadzu 7000). CuK_α (1.541Å) radiation with nickel filter was used. Scanning electron microscopy (SEM) measurements were performed on a Hitachi table top, Model TM 3000. Transmission electron microscopy (TEM) was performed on a Hitachi H-8100 accelerating voltage up to 200 KV, LaB_6 filament equipped with EDS (Kevex sigma TM Quasar, USA). The prepared samples were dispersed on a sticky carbon pad. The thin layer of gold (Au) was deposited on the sample to get better image quality. The diffuse reflectance spectroscopy of the samples was recorded on spectrometer Perkin Elmer (Lambda-35). The Jobin-Yvon spectrofluorimeter fluorolog-3 operational with 450W xenon lamp as an excitation source was used for photoluminescence (PL) measurement.

3. Results and discussion

The SEM images of the optimized Eu^{3+} (4 mol %) doped Ca_2SiO_4 phosphors without EGCG at different sonication times (1, 2, 3, 4, 5 and 6 h) was shown in Fig. 2. By comparing the micrographs of the phosphors by various sonication times, it was evident that ultrasound duration time significantly changes the morphological features. The SEM micrographs of $\text{Ca}_2\text{SiO}_4: \text{Eu}^{3+}$ (4 mol %) nanophosphor obtained for 1 h sonication exhibit an agglomerated particles (Fig.2 (a)). When the ultra-sonication time was increased to 2 h, the needle-like shape morphology was dominated (Fig.2 (b)). However, when the sonication time was increased to 3 h, flower like morphology was obtained (Fig.2 (c)). When increase the reaction time of 4 h showed the formation of large number of long needle-like shaped with well-defined morphology with typical widths of $(30-50) \pm 5 \mu\text{m}$ and lengths in the range of $(80-140) \pm 3 \mu\text{m}$ respectively. Normally in sonochemical synthesis two types' of reactions occur; (i) interaction between cavitation bubble with the surrounding bulk solution leads to crystalline nature and (ii) inside the collapsing bubbles leads to amorphous material. In the present case, crystalline powders with needle like morphology was obtained, hence the formation of the Ca_2SiO_4 was in the interfacial region. The formation mechanism of the needle-like morphology was based on the electrostatic interaction between Ca^{2+} and SiO_4^{4-} ions at the beginning and then followed by their assembly on the surface of micelles. The unstable bubble formed in the liquid-solid interface initially starts collapsing at one weaker surface and then leads to jetting forms the needles like morphology. The mechanism for the formation process of needle-like morphology can be shown schematically illustrated in Fig. 3.

The above-mentioned synthesis procedure was repeated along with 25 ml of EGCG for different time duration. Effect of sonication time on 25 ml optimized EGCG was reported in

Fig. 4. In the presence of EGCG, the uniform, smooth spherical shaped spheres were formed. By comparing the SEM micrographs of with and without EGCG, it can be evident that uniform and smooth spherical shaped was tuned by sonication time.

Further, effect of various concentrations of EGCG (5 - 35 ml) on morphology was studied with fixed sonication time (1 h) and was shown in Fig. 5. It was observed that particles having large agglomeration were noticed for 5ml of EGCG (Fig.5 (a)). However, with increase of EGCG concentration to 10 ml, agglomeration was slightly reduced. Further, with increase of EGCG concentration to 15, 20 ml, the product exhibit smaller and bigger sized spherical particles as observed in Fig. 5 (d & c). When EGCG concentration was 25, 30 and 35 ml, smooth spherical shaped particles were noticed. On the basis of SEM studies, the formation of Ca_2SiO_4 uniform spheres can be explained by a vesicle-template mechanism as shown in Fig. 6. The ultrasonic wave originated the self-aggregation of EGCG molecules to form spherical micelle structures. These micelles were metastable and characterized by active ligands on their surfaces. As EGCG was a cationic surfactant, SiO_4^{4-} ions in the solution were easily attracted to the micelle surface. Thus, the SiO_4^{4-} ion-covered micelles could be formed, which provided nucleation domains for the succeeding reaction between SiO_4^{4-} and Ca^{2+} to form hollow spheres. During ultrasound irradiation of solution, the extreme but transient local conditions affected by acoustic cavitations could not only speed up the dissolution of $\text{Ca}(\text{NO}_3)_2$ to generate Ca^{2+} ions progressively but also facilitate the uniform deposition of the amorphous Ca_2SiO_4 nanophosphors onto the surface of the templates. The micelle template could be effectively extracted by a washing without damaging the spherical structures.

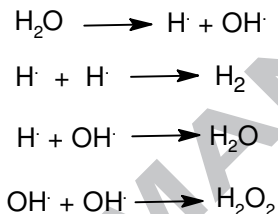
Effect of pH on morphological features was studied by adding ammonia into the reaction mixture (Fig.7a). It was observed that the pH may greatly influence the morphology of the

product. Further, by changing the appropriate pH value of the precursor solution could prominently alter the size and dimension of the assembly units and growth pathway. In the growth stage, many of the tiny assembly units extend to grow into hierarchical superstructures to reduce the surface energy. The actual formation processes was more complicated and may require more studies. Several factors may influence to obtain hierarchical superstructures, including crystal- face attraction, electrostatic and dipolar fields associated with the aggregate, Vander Waals forces, intrinsic structures and external factors. The schematic representation of possible growth mechanisms to end up with various hierarchical superstructures was shown in Fig.7 (b). It was well known that optimized sonication condition normally results in reduced particle sizes, highly uniform in particle distribution and reduction in synthesis time, when compared to conventional routes. Therefore, the effect of sonication power on structures, were performed under different frequencies (20 & 22 kHz). Initially, when the frequency of 20 kHz was applied, the particles observed to spherical and more agglomeration (Figs.8 (a & b)); whereas with increase the frequency of sonication to 22 kHz, a uniform spherical shaped particles were formed (Figs.8 (c & d)).

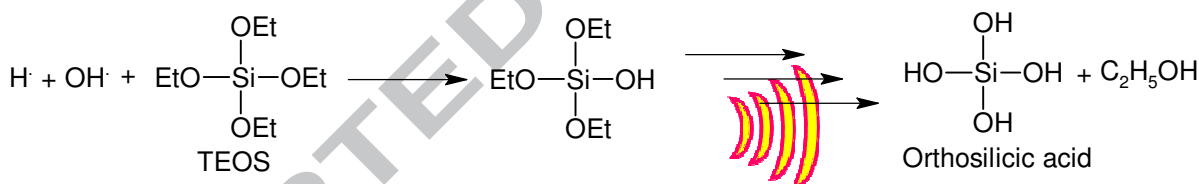
The plausible reaction mechanism for the step by step formation of Ca_2SiO_4 phosphors was given in Fig. 9. Free radical initiated hydrolysis takes place for the formation of metal orthosilicate complex. Initially ultrasonication assisted splitting of water takes place and it reacts with tetraethyl orthosilicate to form orthosilicic acid (H_4SiO_4) (Step 1). Further, hydrolysis may takes place by the replacement of $\text{C}_2\text{H}_5\text{O}^-$ with $-\text{OH}$ group on silicon and four ethanol molecules for the formation of each orthosilicic acid molecule (Step 2). Subsequently, when ionic reaction sets on, resultant H_4SiO_4 with metal nitrate forms respective metal orthosilicate (Step 3). In the final stage a spherical shaped metal orthosilicate particles were observed in the presence of

EGCG (Step 4). It was believed that EGCG play an important role in control the nucleation and growth rate during the reaction. Similar type of interaction of mechanism between EGCG and CdO NPs was proposed in our earlier report [17]. Herein, the EGCG establish a coordinate bond with metal orthosilicate to form micelles and facilitates the typical nucleation (Fig.9). It was assumed that micelles was formed in which coordinated metal with rings B and D diol groups become polar hydrophilic exterior and A and C rings of EGCG hydrophobic and become interior.

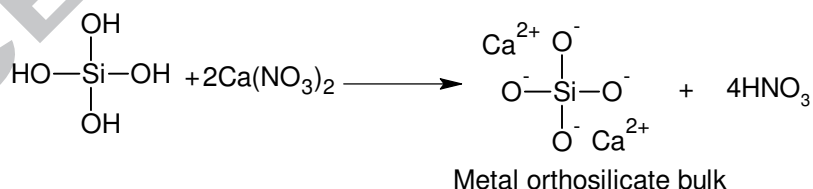
Step 1: Ultrasound irradiation and formation of free radicals



Step 2: Formation of orthosilicic acid



Step 3: Formation of Calcium orthosilicate.



Step 4: Formation of Calcium micro/nano structures.

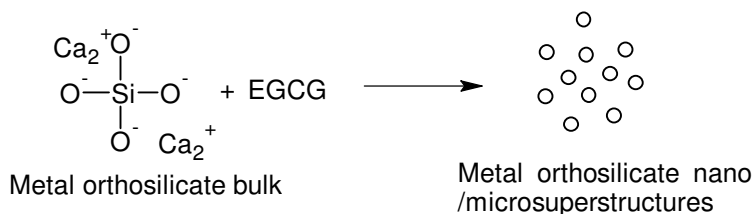


Fig.10. shows TEM and HRTEM images of 6h sonication time, without and with EGCG in $\text{Ca}_2\text{SiO}_4:\text{Eu}^{3+}$ (4 mol %). TEM images clearly evident that the particles were nearly spherical and size was 60 ± 2 nm without EGCG used samples (Fig.10 (a)). Further, the polycrystalline in nature clearly evident in selected area electron diffraction pattern (SAED) (Inset Fig.10 (a)). The interplanar spacing was estimated to be 0.30 ± 0.04 nm (Fig.10 (b)). Fig.10 (c & e) shows the TEM and HRTEM images clearly evident needle and spherical shaped particles with size of around 17 ± 3 nm respectively. The HRTEM images clearly evident the polycrystalline nature with interplanar spacing values of (0.38 ± 0.005) and (0.33 ± 0.002) nm respectively.

Fig.11. shows the PXRD patterns of as formed and calcined $\text{Ca}_2\text{SiO}_4:\text{Eu}^{3+}$ (1 – 5 mol %) nanophosphors. The as formed product was readily indexed to calcium silicate hydrate (JCPDS card no. 33-0306) [14]. The PXRD patterns of calcined $\text{Ca}_2\text{SiO}_4:\text{Eu}^{3+}$ (1 – 5 mol %) at 900°C readily indexed to β -phase which was well matched with JCPDS card no. 36-0642 [14]. Further, no impurity peaks were present in the product indicating that Eu^{3+} and Ca^{2+} ions homogeneously substituted in the host.

The acceptable percentage difference (D_r) between radii of dopant ion Eu^{3+} (0.947 \AA) and substituted ion Ca^{2+} (1.18 \AA) should not be more than 30 % which was obtained by the formula

$D_r = \frac{R_s - R_d}{R_s}$. In the present case estimated value of D_r for $\text{Ca}_2\text{SiO}_4:\text{Eu}^{3+}$ was found to be 19 %.

So, it was believed that the Ca^{2+} was replaced by Eu^{3+} in the host.

The average crystallite size (D) was calculated by using Scherrer's formula,

$$D = \frac{0.89\lambda}{\beta \cos\theta} \quad \text{----- (1)}$$

where D ; the average crystallite size, λ ; the wavelength of the X-rays (0.15405 nm), and θ ; the diffraction angle and β ; full-width at half maximum (FWHM) of the peaks in the PXRD patterns. The average crystalline size (D) was calculated for different Eu^{3+} doped Ca_2SiO_4 nanophosphors were summarized in Table.3. The crystallite size increases with increase of dopant Eu^{3+} concentration which was due to the increase in strain leading the replacement of Ca^{2+} ions by Eu^{3+} ions of smaller radii. To calculate the crystallite size and strain present in the nano/microstructures W–H (Williamson–Hall) fitting method was used [18]. The strain can be estimated by take a slope of the linear fit between $\beta \cos \theta / \lambda$ along y-axis and $\sin \theta / \lambda$ along x-axis and was shown in Fig.12. The estimated values of size and strain were summarized in a Table.3.

Fig.13 shows the diffuse reflectance spectra (DRS) of undoped and Eu^{3+} doped Ca_2SiO_4 nanophosphor recorded in the range 200 - 800 nm at RT. In the shorter wavelength region the spectra exhibit a weak absorption band may be due to formation of meta-stable states between valence band and conduction band by the Eu^{3+} ions due to more absorption of host matrix. The several electronic absorption bands were observed in the longer wavelength region which was assigned from ground state ${}^7\text{F}_0$ to various excited states of Eu^{3+} ions [19]. Due to variation in particle size red shift of the bands were observed in the DR spectra with increase in Eu^{3+} concentration.

The Kubelka–Munk (K-M) theory was utilized to determine the energy band gap (E_g) of synthesized undoped and Eu^{3+} doped Ca_2SiO_4 nanophosphors from DR spectra. The intercept of the tangents to the plots of $[F(R_\infty)h\nu]^{1/2}$ versus photon energy $h\nu$ was shown in Fig. 14. The Kubelka–Munk function $F(R_\infty)$ and photon energy ($h\nu$) was calculated by following equations [20]:

$$F(R_{\infty}) = \frac{(1 - R_{\infty})^2}{2R_{\infty}} \text{-----} (2)$$

$$h\nu = \frac{1240}{\lambda} \times 10^9 \text{ eV} \text{-----} (3)$$

where R_{∞} ; reflection coefficient of the sample, λ ; the absorption wavelength. The calculated band gap energies were summarized in Table.3. The degree of structural order and disorder into the matrix was leads to changes in E_g and also which will change the distribution of energy levels within in the band gap [21]. Furthermore, the degree of structural order–disorder of the matrix was mainly depends on the preparation methods as well as experimental conditions which can favor or slow up the formation of structural defects, which was also cause for the variation in the E_g .

Inset of Fig.15 shows the excitation spectrum of Eu^{3+} doped Ca_2SiO_4 (4 mol %) nanophosphor monitored at 613 nm. The broad band at 261 nm was due to the charge transfer transition of $\text{Eu}^{3+}-\text{O}^{2-}$. The charge transition band was due to the fact that a transfer of electron from 2p orbital of an oxygen to an empty 4f shell of dopant Eu^{3+} ions. The excitation spectra of $\text{Ca}_2\text{SiO}_4: \text{Eu}^{3+}$ exhibit peaks at 299, 320, 360, 381, 393 and 414 nm were attributed to transition of ${}^7\text{F}_0 \rightarrow {}^5\text{F}_3$, ${}^7\text{F}_0 \rightarrow {}^5\text{H}_6$, ${}^7\text{F}_0 \rightarrow {}^7\text{D}_4$, ${}^7\text{F}_0 \rightarrow {}^5\text{L}_7$, ${}^7\text{F}_0 \rightarrow {}^5\text{L}_6$, and ${}^7\text{F}_0 \rightarrow {}^5\text{D}_3$ respectively [19]. According to Jorgensen, the CTB energy (ECT) was proportional to difference in optical electronegativities between ligand anion X and center cation M was given by

$$E_{ct} (\text{cm}^{-1}) = [\chi_{opt}(X) - \chi_{opt}(M)] 30 \times 10^3 \text{ cm}^{-1} \text{-----} (4)$$

where $\chi_{opt}(X)$ and $\chi_{opt}(M)$; optical electronegativities of the ligand and central metal ion respectively, E_{ct} ; the energy of charge transfer band. Substituting the values of $\chi_{opt}(X) = 3.38$ and $\chi_{opt}(M)(\text{Eu}^{3+}) = 1.78$ into Eq. (4), the position of $\text{O}^{2-} \rightarrow \text{Eu}^{3+}$ CTB can be calculated to be 208 nm. It clearly shows that Ca_2SiO_4 nanophosphor may be an efficient host and sensitizer with

an energy transfer from O^{2-} to Eu^{3+} ions. The Eu^{3+} ions were widely used as luminescence activators with an emission of red light and it was a promising structural probe. The energy level of Eu^{3+} ions arises from the $4f - 4f$ transition and was shown in Fig.16. The PL emission spectrum of Eu^{3+} doped Ca_2SiO_4 nanophosphor was sensitive to the surrounding environment. The transition ${}^5D_0 \rightarrow {}^7F_1$ due to magnetic dipole will be dominate when inversion symmetry site was occupied by Eu^{3+} ions [22]. In contrast, the transition ${}^5D_0 \rightarrow {}^7F_2$ due to electric dipole will be dominate when non-centrosymmetric site was occupied by Eu^{3+} ions [23]. In the present case Eu^{3+} ions embedded in non-inversion centrosymmetric of hosts. Therefore, a red emission intensity due to ${}^5D_0 \rightarrow {}^7F_2$ was dominate than that of orange emission intensity due to ${}^5D_0 \rightarrow {}^7F_1$ in Eu^{3+} doped Ca_2SiO_4 nanophosphor.

The PL emission spectra of Eu^{3+} doped Ca_2SiO_4 nanophosphor was recorded at $\lambda_{exc}=393$ nm. Emission spectra exhibit five peaks at 570, 593, 613, 654 and 702 nm which were attributed to ${}^5D_0 \rightarrow {}^7F_0$, ${}^5D_0 \rightarrow {}^7F_1$, ${}^5D_0 \rightarrow {}^7F_2$, ${}^5D_0 \rightarrow {}^7F_3$ and ${}^5D_0 \rightarrow {}^7F_4$; $4f^6$ configuration of Eu^{3+} ions, respectively [24, 25]. In emission spectra, the narrow bands were due to electron shielding effect in rare-earth ions (Eu^{3+}). The intensive peak at 613 nm was attributed to the hypersensitive transition between the 5D_0 and 7F_2 levels of the Eu^{3+} in the host Ca_2SiO_4 matrix aroused due to a forced electric dipole transition. The weak emission peak at 593 nm attributed to of ${}^5D_0 \rightarrow {}^7F_1$ transition ascribed to magnetic dipole transition and was insensitive to site symmetry. To measure the degree of distortion from the inversion symmetry of the local environment of the Eu^{3+} ions in the host matrix, the asymmetric ratio (A_{21}) was an important parameter [26];

$$A_{21} = \frac{\int I_2({}^5D_0 \rightarrow {}^7F_1) d\lambda}{\int I_1({}^5D_0 \rightarrow {}^7F_2) d\lambda} \quad \text{----- (5)}$$

where I_1 and I_2 ; intensity of magnetic dipole transition at 593 nm and electric dipole transition at 613 nm respectively. Therefore the value of A_{21} for $\text{Ca}_2\text{SiO}_4:\text{Eu}^{3+}$ increases in the beginning then it decreases with further increase in Eu^{3+} concentration (Fig. 17). The effect of various Eu^{3+} concentrations on the PL intensity of $\text{Ca}_2\text{SiO}_4:\text{Eu}^{3+}$ nanophosphor was studied and shown in Fig.17. In the present case, PL intensity increased with increase in Eu^{3+} concentration up to 4 mol % and afterwards it starts decreases due to concentration quenching. The origin of concentration quenching phenomena may be explained based on [27]:

- (i) Defect to Eu^{3+} energy transfer.
- (ii) Electron-phonon coupling and multiphonon assisted energy transfer.
- (iii) Eu^{3+} - Eu^{3+} energy transfer.

Due to the absence of defect to Eu^{3+} energy transfer transition in the present work indicating that this type of energy transfer mechanism was not responsible for concentration quenching phenomena. In the excitation spectrum of $\text{Ca}_2\text{SiO}_4:\text{Eu}^{3+}$ nanophosphor weak bands between 380 - 450 nm due to transitions ${}^7\text{F}_0 \rightarrow {}^5\text{D}_2$ and ${}^7\text{F}_0 \rightarrow {}^5\text{D}_3$ was shown in Fig. 18. The transition ${}^7\text{F}_0 \rightarrow {}^5\text{D}_2$ was a pure electric dipole (PED) transition, it is clear from energy level of Eu^{3+} that energy difference between ${}^5\text{D}_2$ and ${}^5\text{D}_3$ (2500 cm^{-1}) was much larger than vibrational energies of chemical bonds in inorganic compounds [28]. Hence, weak bands between the transitions were due to the phonon-assisted (one or multi-phonon) transition. In multi-phonon process, the nonradiative rate W_{NR} can be calculated by using the modified exponential energy-gap equation of Van Dijk and Schuurmans [29];

$$W_{NR} = \beta_{el} \exp[-\alpha(\Delta E - 2\hbar\omega_{\max})] \quad \text{----- (6)}$$

where β_{el} (10^7 s^{-1}) and α ($4.5 \times 10^{-3} \text{ cm}$); constants respectively and $\hbar\omega_{\max}$; the energy of the active phonons. The calculated multiphonon relaxation was found to be 240 s^{-1} and was very small and not responsible for the concentration quenching in RE ion doped materials.

Huang–Rhys factor S was used to characterize the phonon-assisted transition (PAT) for determine nonradiative transition given by the relation [30];

$$S = \frac{I_{PAT}}{I_{ZP}} \quad \text{----- (7)}$$

where I_{PAT} and I_{ZP} ; the integrated intensities of the phonon-assisted transition and zero phonon line, respectively. The calculated Huang–Rhys factor S was found to be 0.25, which was greater than expected value. The value of the Huang–Rhys factor proves the existence of week electron-phonon coupling between Eu^{3+} dopant and Ca_2SiO_4 host. Thus multiphonon assisted energy transfer was not due the cause of quenching. Hence it may be concluded that the nonradiative energy transfer between rare earth Eu^{3+} ions was reason for concentration quenching. The nonradiative energy transfer between Eu^{3+} was mainly due to exchange interaction, radiationreabsorption, or a multipole–multipole interaction. The self-quenching of Eu^{3+} ions can happen when the separation between two closest Eu^{3+} ions was such that the interaction between the two Eu^{3+} ions was conceivable which leads to increase in the nonradiative relaxation and diminish the luminescence intensity. Initially, the PL intensity increases and then decreases due to smaller radius of Eu^{3+} as compared to Ca^{2+} ions but at higher intensity the charge imbalance leads to cross relaxation and on radiative transitions causes concentration quenching [31]. At higher concentration of Eu^{3+} ions the distance between the activator ions decreases which leads to the non-radioactive energy transfer among Eu^{3+} ions. In this context, the critical distance (R_c) can be estimated from the following equation [32]:

$$R_c \approx 2 \left(\frac{3V}{4\pi X_c N} \right)^{\frac{1}{3}} \quad \text{----- (8)}$$

where V ; the volume of the unit cell, X_c ; the critical concentration Eu^{3+} ions and N ; the number of sites in the unit cell. The schematic representation of Blasse’s formula was shown in Fig.19.

Presently, V ; 342.69 \AA^3 , X_c ; about 0.04 and N ; 4, resulting in the critical distance of $(15.99 \pm 0.007) \text{ \AA}$. The calculated value of R_c was greater than 5 \AA for the Eu^{3+} ions results that the multi-pole–multi-pole interactions in the Ca_2SiO_4 host [33]. Suppose electric multipolar interaction was responsible in the energy transfer, there were several types of interactions may be possible namely dipole–dipole (d–d), dipole–quadrupole (d–q), quadrupole–quadrupole (q–q), etc. Therefore it was a necessity to reveal which type of interaction responsible in the energy transfer. Dexter and Schulman [33] stated that the multi- polar interaction intensity can be resolved based on the change in the emission intensity from the emitting level that has multipolar interaction. The ratio emission intensity (I) to concentration of activator ion follows the equation;

$$\frac{I}{\chi} = K \left[1 + \beta(\chi)^{\frac{Q}{3}} \right]^{-1} \quad \text{----- (9)}$$

Where χ ; the activator concentration, Q ; a constant of multi- polar interaction and equals 6,8, or 10 and less than 6 for dipole–dipole; dipole– quadrupole or quadrupole–quadrupole interactions and charge transfer mechanism respectively, and K and β ; constants for the given host lattice under the same excitation condition.

$$\text{Log } \frac{I}{\chi} = A - \frac{Q}{3} \log \chi \quad \text{----- (10)}$$

where $(A = \log k - \log \beta)$. The curve of $\log I/\chi$ v/s $\log \chi$ in $\text{Ca}_2\text{SiO}_4:\text{Eu}^{3+}$ phosphor was shown in Fig. 20 and clearly confirms that the relation was approximately linear and the value of slope was ~ -1.946 . The calculated value Q was found to be ~ 5.8 was nearly equal to 6. This result indicates that the charge transfer mechanism was due to dipole-dipole interaction for the concentration quenching observed in $\text{Ca}_2\text{SiO}_4:\text{Eu}^{3+}$ phosphor.

Fig.21 shows Commission International De I-Eclairage (CIE) 1931 chromaticity diagram [34, 35] for $\text{Ca}_2\text{SiO}_4:\text{Eu}^{3+}$ (1 - 5 mol %) nanophosphors. The CIE co-ordinates were calculated

using PL emission spectra at the excitation of 393 nm and the values were summarized in a Table.4. It was noticed that the CIE co-ordinates ($x = 0.6185$, $y = 0.3810$) for 4 mol % was located in red region and nearly same as the National Television System Committee (NTSC) standard values of pure red color (0.67, 0.33). By varying the concentration of Eu^{3+} ions from 1 to 5 mol %, color tuning can be observed (shown in the inset of Fig. 21). The correlated color temperature (CCT) was one the important parameter to know the color appearance of the light emitted by a source, relating its color with respect to a reference light source when heated up to a specific temperature in K [36]. CCT was calculated by transforming the (x , y) coordinates of the light source to (U_0 , V_0) by using the following relations, and by determining the temperature of the closest point of the Planckian locus to the light source on the (U_0 , V_0) uniform chromaticity diagram (Fig.22) [37]:

$$U' = \frac{4x}{-2x + 12y + 3} \quad \text{----- (11)}$$

$$V' = \frac{9y}{-2x + 12y + 3} \quad \text{----- (12)}$$

Also, the quality of white light in terms of color correlated temperature (CCT) was given by McCamy empirical formula $CCT = -437 n^3 + 3601 n^2 - 6861 n + 5514 .31$ (theoretical) where $n = (x - x_c)/(y - y_c)$; the inverse slope line and chromaticity epicenter was at $x_c = 0.3320$ and $y_c = 0.1858$ [38]. Values of CCT calculated for each sample was summarized in Table.4. The obtained values were well acceptable range and may be useful in home appliances. Any nanophosphor material can be distinguished by their dominant wavelength and colour purity. This conception was most useful for the narrow banded light sources. The CCT calculation was

most useful broad banded light sources. The color purity of the emitted light from the Ca_2SiO_4 host can estimate by following equation [39]:

$$\text{color purity} = \frac{\sqrt{(x_s - x_i)^2 + (y_s - y_i)^2}}{\sqrt{(x_d - x_i)^2 + (y_d - y_i)^2}} \times 100\% \quad \text{-----} \quad (13)$$

where (x_s, y_s) ; the coordinates of a sample point, (x_d, y_d) ; the coordinates of the dominant wavelength and (x_i, y_i) ; the coordinates of the illuminant point. The estimated values were given in Table.4, which indicated that purity of the red color increases with increase of Eu^{3+} concentration.

The intensity parameters were calculated by using Judd-Ofelt theory for the study of site symmetry and luminescence behavior of rare earth doped host matrix [40, 41]. Previously, these parameters were calculated by using absorption spectra. However, in the present case emission spectra has been used for estimation of intensity parameters. The relation between radiative emission rates and the integrated emission intensities was given by the equation [42]:

$$\frac{A_{0-2,4}}{A_{0-1}} = \frac{I_{0-2,4}}{I_{0-1}} = \frac{h\nu_{0-1}}{h\nu_{0-2,4}} \quad \text{-----} \quad (14)$$

where I_{0-J} and $h\nu_{0-J}$; integrated emission intensity and energies corresponding to transition ${}^5D_0 \rightarrow {}^7F_J$ ($J = 1, 2, 4$) respectively.

The radiative transition rates (A_{0-J}) of electric dipole is expressed as

$$A_{(0-J)} = \frac{64\pi^4 \bar{\lambda}_J^3}{3h(2J+1)} \frac{n(n^2+2)^2}{9} \sum_{\lambda=2,4} \Omega_\lambda \left| \left\langle {}^5D_0 \left\| U^{(\lambda)} \right\| {}^7F_J \right\rangle \right|^2 \quad \text{-----} \quad (15)$$

where $A_{(0-J)}$; the coefficient of spontaneous emission, e ; the electronic charge, $\bar{\lambda}_J$; the wave number of the corresponding transition, h ; the Planck's constant, S_{md} ; the strength of the magnetic dipole and n ; the RI of the prepared sample. $\left| \left\langle {}^5D_0 \left\| U^{(\lambda)} \right\| {}^7F_J \right\rangle \right|^2$; squared reduced

matrix element of Eu^{3+} and were 0.0032 and 0.0023 for $J = 2$ and 4 respectively and these value was independent of the chemical environment [42]. Thus, by using Eqs. (14) and (15), the values of Ω_2 and Ω_4 were tabulated in a Table. 5. The variation in the value of Ω_2 with different Eu^{3+} concentration specifies that Ω_2 was more sensitive to the ligand environment. The parameter Ω_2 shows its dependence on the covalency between rare earth ions and ligand anions because parameter Ω_2 replicates the asymmetry of the local environment at the Eu^{3+} ion site. The increase in the value of Ω_2 with concentration shows a decrease in the symmetric nature of Eu^{3+} in this host. The radiative properties such as transition probabilities (A_T), radiative lifetimes (τ_{rad}) and branching ratios (β_R) for the excited states of Eu^{3+} ions were calculated by using estimated values of J–O parameters with the following equations [39, 43].

$$A_T(\psi J) = \sum_{J'} A_{J-J'} \quad \text{----- (16)}$$

$$\tau_{\text{rad}}(\psi J) = \frac{1}{A_T(\psi J)} \quad \text{----- (17)}$$

$$\beta(\psi J) = \frac{A(\psi J, \psi' J')}{A_T(\psi J)} \quad \text{----- (18)}$$

The measured branching ratio for Eu^{3+} doped Ca_2SiO_4 nanophosphor to be $0.99 \geq 0.50$ suggests that the present nanophosphor can emit laser radiation more effectively and is suitable for displaying devices.

4. Conclusions

A series of red emitting $\text{Ca}_2\text{SiO}_4:\text{Eu}^{3+}$ (1– 5 mol %) nanophosphors were prepared by facile EGCG assisted ultrasound method. The hierarchical superstructures largely depend on sonication time, pH and concentration of EGCG. The growth mechanism of spherical, hierarchical superstructures was proposed. The PXRD patterns of phosphors calcined at 950 °C confirms single β -phase of Ca_2SiO_4 . The energy gap (E_g) value varies from 4.69–5.16 eV. The phosphor exhibit intense red emission assigned for the transition ($^5\text{D}_0 \rightarrow ^7\text{F}_2$) at 613 nm. PL intensity increases up to 4 mol % and then diminishes due to self-quenching effect. The optimized red emitting phosphor exhibited high efficiency and color purity. Further, the phosphor showed CIE chromaticity co-ordinates and CCT values which are very close to the values of standard red phosphors. Hence, the phosphor obtained by ultrasound route may be useful for display and solid state lightning applications.

Acknowledgement

The author Dr. H Nagabhushana thanks to DST Nano Mission New Delhi for the sanction of this Project.

ACCEPTED MANUSCRIPT

References

1. K. S. Suslick, The chemical Effect of Ultrasound, *Sci. Am.* 260 (1989) 80-86.
2. Jin Ho Bang, Kenneth S. Suslick, Applications of Ultrasound to the Synthesis of Nanostructured Materials *Adv. Mater.* 22 (2010) 1039–1059.
3. J. R. Agger, M. W. Anderson, M. E. Pemble, O. Terasaki, Y. Nozue, Growth of quantum-confined indium phosphide inside MCM-41. *J. Phys. Chem. B*, 102(1998) 3345–3353.
4. Srirupa Mukherjee, Dimple P. Dutta, N. Manoj, A. K. Tyagi, Sonochemically synthesized rare earth double-doped zirconia nanoparticles: probable candidate for white light emission, *J. Nanopart. Res.* 14 (2012) 814-815.
5. T. Justel, H. Nikol, C. Ronda, New developments in the Field of Luminescent materials for Lightning and Displays, *Angew. Chem. Int. Ed.* 37 (1998) 3084-3103.
6. B. Jaya Raja , M. Rajesh Yadav, V. PushpaManjari, B. Babu, Ch. Rama Krishna, R.V.S.S.N. Ravikumar, Synthesis and characterization of undoped and Mn(II) ions doped $\text{Li}_2\text{Ca}_4\text{Al}_4(\text{PO}_4)_4\text{F}_4$ nanophosphors, *J. Mol. Struct.* 1076 (2014) 461–467.
7. Chun Che Lin, Andries Meijerink, Ru-Shi Liu, Critical Red Components for Next-Generation White LEDs, *J. Phys. Chem. Lett.*, 7(2016) 495–503.
8. L. Lin, M. Yin, C. S. Shi, W. P. Zhang, Luminescence properties of a new red long-lasting phosphor: $\text{Mg}_2\text{SiO}_4:\text{Dy}^{3+}, \text{Mn}^{2+}$, *J. Alloys Comp.* 455 (2008) 327–330.
9. T.G.V.M. Rao, A. Rupesh Kumar, N. Veeraiah, M. Rami Reddy, Optical and structural investigation of $\text{Sm}^{3+}\text{-Nd}^{3+}$ co-doped in magnesium lead borosilicate glasses, *J. Phys. Chem. Solid.* 74 (2013) 410-417.

10. Hao Feng, Yang Yang, Xiuguo Zhang, Yongchun Xu, Jinyu Guan, Synthesis and luminescence of $\text{Sr}_2\text{SiO}_4:\text{Eu}^{3+}$ micro-spherical phosphors by a spray-drying process, *Superlattices and Microstructures* 78 (2015) 150–155.
11. H. Nagabhushana, D.V. Sunitha, S.C. Sharma, B. Daruka Prasad, B.M. Nagabhushana, R.P.S. Chakradhar, Enhanced luminescence by monovalent alkali metal ions in $\text{Sr}_2\text{SiO}_4:\text{Eu}^{3+}$ nanophosphor prepared by low temperature solution combustion method, *J. Alloys Compd.* 595 (2014) 192–199.
12. Sakthivel Gandhi, Kavitha Thandavan, Bong-Joon Kwon, Hyun-Joo Woo, Kiwan Jang, Dong-Soo Shin, Solvothermal synthesis of red and green emitting $\text{Ca}_{1.65}\text{Sr}_{0.35}\text{SiO}_4:\text{Eu}^{3+}$ and $\text{Ca}_{1.65}\text{Sr}_{0.35}\text{SiO}_4:\text{Eu}^{2+}$ phosphors for solid-state lighting applications, *Ceram. Int.* 40 (2014) 5245–5254.
13. Nur Alia Sheh Omar, Yap Wing Fen, Khamirul Amin Matori, Photoluminescence properties of Eu^{3+} doped low cost zinc silicate based glass ceramics, *Optik* 127 (2016) 3727–3729.
14. D.V. Sunitha, H. Nagabhushana, S.C. Sharma, B.M. Nagabhushana, R.P.S. Chakradhar, Luminescent characteristics of Eu^{3+} doped di-calcium silicate nano-powders for white LEDs, *J. Alloys Compd.* 575 (2013) 434–443.
15. Ramachandra Naik, S.C. Prashantha, H. Nagabhushana, S.C. Sharma, B.M. Nagabhushana, H.P. Nagaswarupa, H.B. Premkumar, Low temperature synthesis and photoluminescence properties of red emitting $\text{Mg}_2\text{SiO}_4:\text{Eu}^{3+}$ nanophosphor for near UV light emitting diodes, *Sensors and Actuators B*, 195 (2014) 140–149.
16. S.A.H. Tabrizi, E. Taheri-Nassaj, Polyacrylamide gel synthesis and sintering of $\text{Mg}_2\text{SiO}_4:\text{Eu}^{3+}$ nanopowder, *Ceram. Int.* 39 (2013) 6313–6317.

17. H. Nagabhushana, R.B. Basavaraj, B. Daruka Prasad, S.C. Sharma, H.B. Premkumar, Udayabhanu, G.R. Vijayakumar, Facile EGCG assisted green synthesis of raspberry shaped CdO nanoparticles, *J. Alloys Compd.* 669 (2016) 232-239.
18. G.P. Darshan, H.B. Premkumar, H. Nagabhushana, S.C. Sharma, S.C. Prashanth, B. Daruka Prasad, Effective finger print recognition technique using doped yttrium aluminate nano phosphor material, *J. Coll. Inter. Sci.* 464 (2016) 206-218.
19. Xinguo Zhang, Mengyang Chen, Jilin Zhang, Xinzhen Qin, Menglian Gong, Photoluminescence studies of high-efficient red-emitting $K_2Y(WO_4)(PO_4):Eu^{3+}$ phosphor for NUV LED, *Mater. Res. Bull.* 73 (2016) 219–225.
20. A. E. Morales, E. S. Mora and U. Pal, Use of diffuse reflectance spectroscopy for optical characterization of un-supported nanostructures, *Rev. Mex. Fis.* 53 (2007) 18-22.
21. Ramachandra Naik, S.C. Prashantha, H. Nagabhushana, H.P. Nagaswarupa, K.S. Anantharaju, S.C. Sharma, B.M. Nagabhushana, H.B. Premkumar, K.M. Girish, $Mg_2SiO_4:Tb^{3+}$ nanophosphor: Auto ignition route and near UV excited photoluminescence properties for WLEDs, *J. Alloys Compd.* 617(2014) 69-75.
22. N. Zhang, C. Guo, L. Yin, J. Zhang, M. Wu, Red emitting phosphors of Eu^{3+} doped $Na_2Ln_2Ti_3O_{10}$ (Ln = Gd, Y) for white light emitting diodes, *J. Alloys Compd.* 635 (2015) 66–72.
23. H. Yu, H. Song, G. Pan, S. Li, Z. Liu, X. Bai, T. Wang, H. Zhao, Preparation and luminescent properties of europium-doped yttria fibers by electrospinning, *J. Lumin.* 124 (2007) 39–44.
24. S. Som, A. K. Kunti, Vinod Kumar, Vijay Kumar, S. Dutta, M. Chowdhury, S. K. Sharma, J. J. Terblans, H. C. Swart, Defect correlated fluorescent quenching and electron

- phonon coupling in the spectral transition of Eu^{3+} in CaTiO_3 for red emission in display application *J. Appl. Phys.* 115(2014) 193101-193114.
25. LI Mengting, JIAO Baoxiang, Synthesis and photoluminescence properties of $\text{ZnTiO}_3:\text{Eu}^{3+}$ red phosphors via sol-gel method, *J. Rare Earths*, 33 (2015)231-238.
 26. M. Chandrasekhar, H. Nagabhushana, S.C. Sharma, K.H. Sudheerkumar, N. Dhananjaya, D.V. Sunitha, C. Shivakumara, B.M. Nagabhushana, Particle size, morphology and color tunable $\text{ZnO}:\text{Eu}^{3+}$ nanophosphors via plant latex mediated green combustion synthesis, *J. Alloys Compd.* 584 (2014) 417– 424.
 27. P. Boutinaud, L. Sarakha, E. Cavalli, M. Bettinelli, P. Dorenbos, R. Mahiou, About red after glow in Pr^{3+} doped titanate perovskites, *J. Phys. D: Appl. Phys.* 42, (2009)045106.
 28. J. M. F. Van Dijk and M. F. H. Schuurmans, On the non-radiative and radiative decay rates and a modified exponential energy gap law for $4f-4f$ transitions in rare-earth ions, *J. Chem. Phys.* 78 (1983) 5317.
 29. H. You, G. Hong, The change of Eu^{3+} surroundings in the system $\text{Al}_2\text{O}_3-\text{B}_2\text{O}_3$ containing Eu^{3+} ions *J. Phys. Chem. Solids*, 60(1999) 325-329.
 30. S. Dutta, S. Som, S. K. Sharma, Luminescence and photometric characterization of K^+ compensated $\text{CaMoO}_4:\text{Dy}^{3+}$ nanophosphors, *Dalton Trans.*, (2013) 9654-9664.
 31. G. Blasse, Energy transfer between inequivalent Eu^{2+} ions, *J. Solid State Chem.* 62 (1986) 207-211.
 32. G. Blasse and B. C. Grabmarier, *Luminescent Materials* (Springer-Verlag, Berlin, 1994), p. 99.
 33. D. L. Dexter and J. H. Schulman, Theory of concentration quenching in inorganic phosphors, *J. Chem. Phys.* 22(6) (1954) 1063–1070.

34. Publication CIE no 17.4 (1987) International Lighting Vocabulary, Central Bureau of the Commission Internationale de L 'Eclairage, Vienna, Austria.
35. Publication CIE no 15.2 (1986) Colorimetry, Second Edition, Central Bureau of the Commission Internationale de L 'Eclairage, Vienna, Austria.
36. János Schanda, M Danyi, Correlated Color-Temperature Calculations in the CIE 1976 Chromaticity Diagram, *Color Res. Appl.* 2 (1977) 161-163.
37. K.M. Girish, Ramachandra Naik, S.C. Prashantha, H. Nagabhushana, H. P Nagaswarupa, K.S. AnathaRaju, H.B. Premakumar, S.C. Sharma, B. M. Nagabhushana, $\text{Zn}_2\text{TiO}_4:\text{Eu}^{3+}$ nanophosphor: Self explosive route and its near UV excited photoluminescence properties for WLEDs, *Spectrochim. Acta Part A*, 138 (2015) 857-865.
38. C.S. McCamy, Correlated color temperature as an explicit function of chromaticity coordinates, *Color Res. Appl.* 17 (1992) 142-144.
39. S. Som, Subrata Das, S. Dutta, Hendrik G. Visser, Mukesh Kumar Pandey, Pushpendra Kumar, Ritesh Kumar Dubey, S. K. Sharma, Synthesis of strong red emitting $\text{Y}_2\text{O}_3:\text{Eu}^{3+}$ phosphor by potential chemical routes: comparative investigations on the structural evolutions, photometric properties and Judd–Ofelt analysis, *RSC Adv.* 5 (2015) 70887-70898.
40. B. R. Judd, Optical absorption intensities of rare-earth ions, *Phys Rev.* 127(1962) 750.
41. G S Ofelt, Intensities of crystal spectra of rare-earth ions, *J. Chem. Phys.* 37 (1962) 37, 511-520.
42. J. Feng, H. Zhang, Hybrid materials based on lanthanide organic complexes: a review *Chem. Soc. Rev.* 42 (2013) 387-410.
43. C. A. Kodaira, H. F. Brito, O. L. Malta, Luminescence and energy transfer of the europium (III) tungstate obtained via the Pechini method, *J. Lumin.* 101 (2003) 11–21.

Figure Captions:

Fig.1.Schematic for the synthesis of Eu^{3+} doped Ca_2SiO_4 nanophosphor by ultrasonication method.

Fig.2.SEM images of $\text{Ca}_2\text{SiO}_4:\text{Eu}^{3+}$ (4 mol %) nanophosphor with different sonication times (1, 2, 3, 4, 5 and 6 hrs) without EGCG.

Fig.3.Schematic representation of formation process of needle - like morphology in $\text{Ca}_2\text{SiO}_4:\text{Eu}^{3+}$ (5 mol %) nanophosphor.

Fig.4. SEM images of $\text{Ca}_2\text{SiO}_4:\text{Eu}^{3+}$ (4 mol %) nanophosphor with different sonication times (1, 2, 3, 4, 5 and 6 hrs) with EGCG (25 ml).

Fig.5. SEM images of $\text{Ca}_2\text{SiO}_4:\text{Eu}^{3+}$ (4 mol %) nanophosphor with different concentration of EGCG (10, 15, 20, 25, 30 and 35 ml) with 1hr of ultrasonic irradiation time.

Fig.6.Schematic representation of formation process of hollow spheres morphology in $\text{Ca}_2\text{SiO}_4:\text{Eu}^{3+}$ (4 mol %) nanophosphor.

Fig.7 (a).SEM images of $\text{Ca}_2\text{SiO}_4:\text{Eu}^{3+}$ (4 mol %) nanophosphor with various pH values (5, 7, 9, 11 and 12) with 1hr of ultrasonic irradiation time.

Fig.7 (b).Schematic representation for the formation of hierarchical superstructures of $\text{Ca}_2\text{SiO}_4:\text{Eu}^{3+}$ (4 mol %) nanophosphor with various pH values.

Fig.8. SEM images of $\text{Ca}_2\text{SiO}_4:\text{Eu}^{3+}$ (4 mol %) nanophosphor with different sonication power (20 and 22 kHz).

Fig.9. Schematic representation of $\text{Ca}_2\text{SiO}_4:\text{Eu}^{3+}$ nanostructures in the presence of EGCG.

Fig.10. TEM and HRTEM images of $\text{Ca}_2\text{SiO}_4:\text{Eu}^{3+}$ (5 mol %) nanophosphor.

Fig.11(a). PXRD patterns of as formed and $\text{Ca}_2\text{SiO}_4:\text{Eu}^{3+}$ (1–5 mol %) nanophosphor.

Fig.12. W–H plots of $\text{Ca}_2\text{SiO}_4:\text{Eu}^{3+}$ (1–5 mol %) nanophosphor.

Fig.13. Diffuse reflectance spectra of undoped and $\text{Ca}_2\text{SiO}_4:\text{Eu}^{3+}$ (1–5 mol %) nanophosphor.

Fig.14.Energy band gaps of undoped and $\text{Ca}_2\text{SiO}_4:\text{Eu}^{3+}$ (1–5 mol %) nanophosphor.

Fig.15. PL emission spectra of $\text{Ca}_2\text{SiO}_4:\text{Eu}^{3+}$ (1–5 mol %) nanophosphor at $\lambda_{\text{exc}}= 393\text{nm}$. Inset shows the PL excitation spectra of $\text{Ca}_2\text{SiO}_4:\text{Eu}^{3+}$ (4 mol%) nanophosphor at $\lambda_{\text{emi}}= 613\text{nm}$.

Fig.16.Energy levels diagram of Eu^{3+} doped Ca_2SiO_4 nanophosphor.

Fig.17. Effect of concentration of Eu^{3+} on the 613 nm emission and the variation of asymmetric ratio in Ca_2SiO_4 nanophosphors.

Fig.18. PL excitation spectrum, with the enlarged portion, showing the phonon-assisted transition.

Fig.19. The schematic representation of Blasse's relation.

Fig.20. Relation between $\log(x)$ and $\log(I/x)$ in $\text{Ca}_2\text{SiO}_4:\text{Eu}^{3+}$ (1–5 mol %) nanophosphor.

Fig.21. CIE diagram of $\text{Ca}_2\text{SiO}_4:\text{Eu}^{3+}$ (1–5 mol %) nanophosphor.

Fig.22. CCT diagram of $\text{Ca}_2\text{SiO}_4:\text{Eu}^{3+}$ (1–5 mol %) nanophosphor.

ACCEPTED MANUSCRIPT

Table Captions:

Table.1. Method of preparation, formation temperature and morphology of the product obtained in various silicate phosphors.

Table.2.The chemicals used in the present study.

Table 3: Estimated crystallite size, strain and energy gap (E_g) values of $\text{Ca}_2\text{SiO}_4:\text{Eu}^{3+}$ (1-5mol %) nanophosphor.

Table.4. Photometric characteristics of Eu^{3+} doped Ca_2SiO_4 nanophosphors.

Table 5: Judd-Ofelt intensity parameters (Ω_2, Ω_4), Emission peak wavelengths (λ_p in nm), radiative transition probability (A_T), calculated radiative (τ_{rad}) lifetime, branching ratio (β_R) and asymmetric ratio (A_{21}) of $\text{Ca}_2\text{SiO}_4:\text{Eu}^{3+}$ (1-5mol%) compounds ($\lambda_{\text{ex}} = 393$ nm).

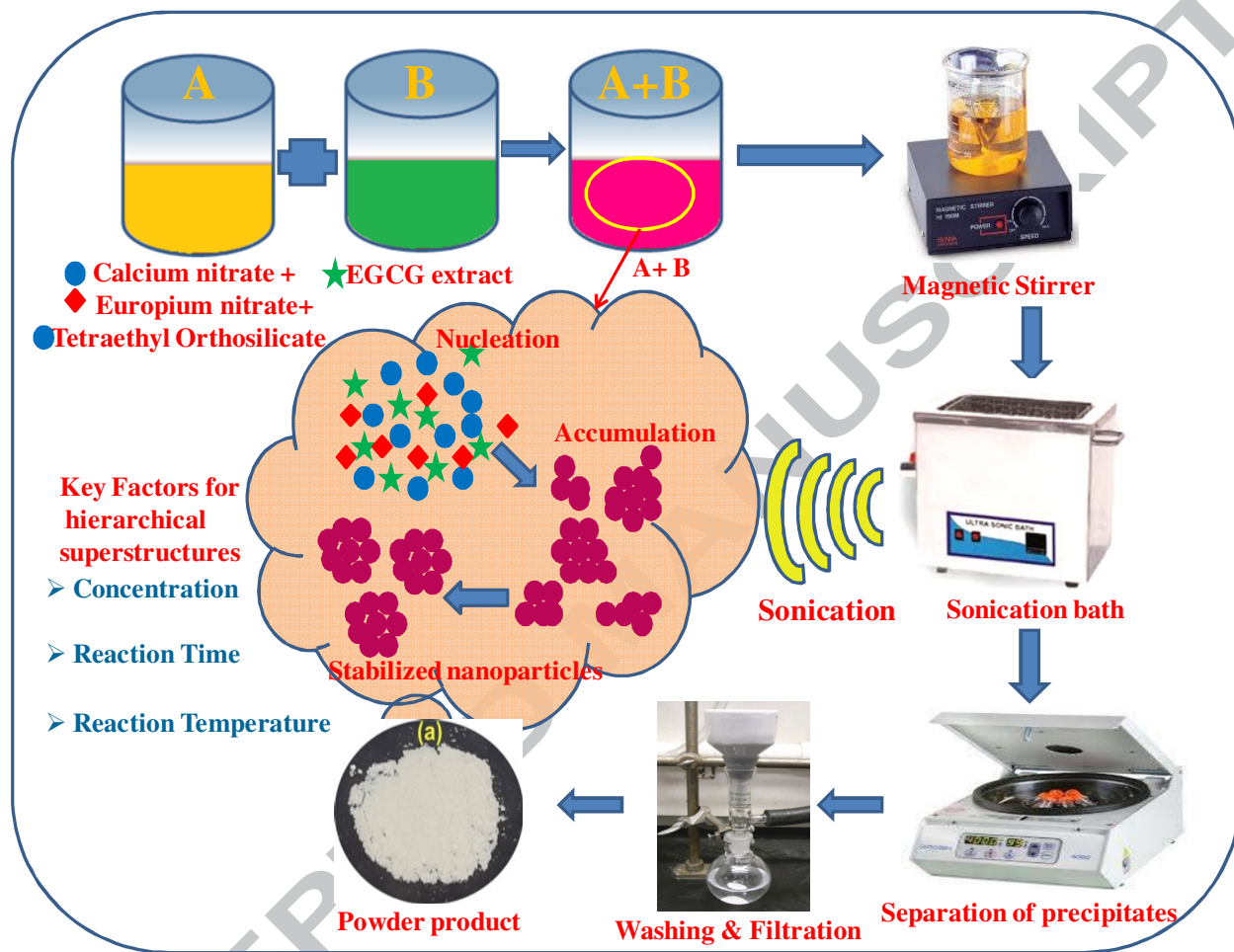


Fig.1. Schematic for the synthesis of Eu^{3+} doped Ca_2SiO_4 nanophosphor by ultrasonication method.

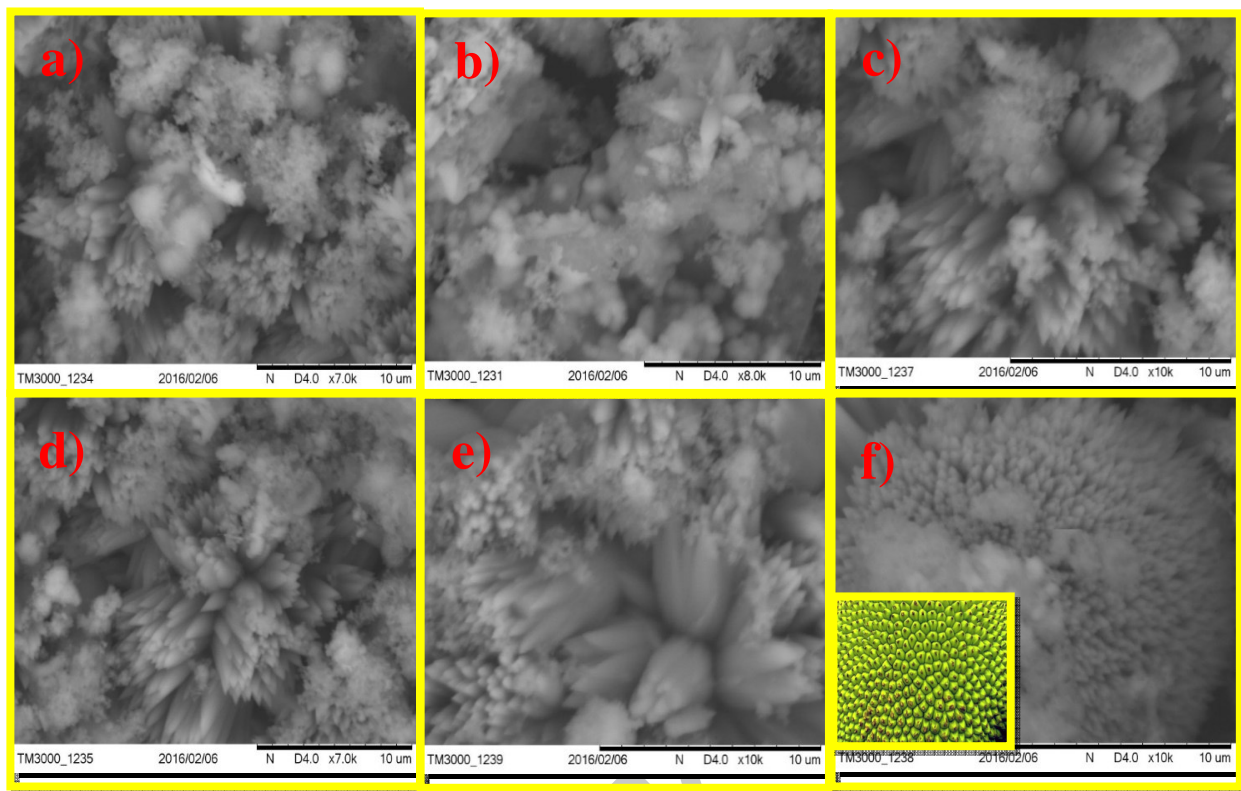


Fig.2. SEM images of $\text{Ca}_2\text{SiO}_4: \text{Eu}^{3+}$ (4 mol %) nanophosphor with different sonication times (1, 2, 3, 4, 5 and 6 hrs) without EGCG.

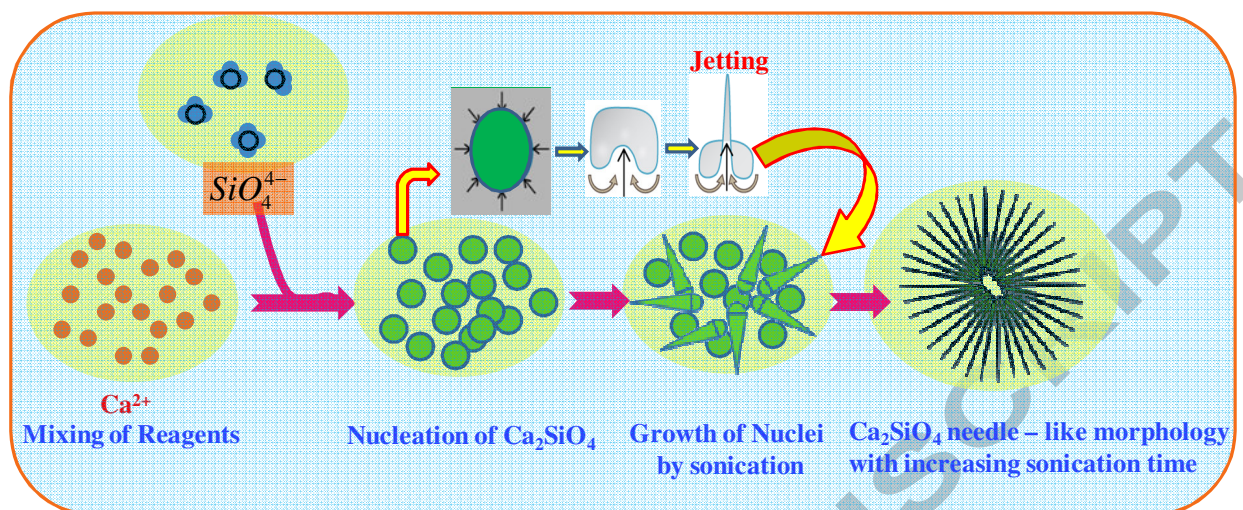


Fig.3. Schematic representation of formation process of needle - like morphology in Ca_2SiO_4 : Eu^{3+} (4 mol %) nanophosphor.

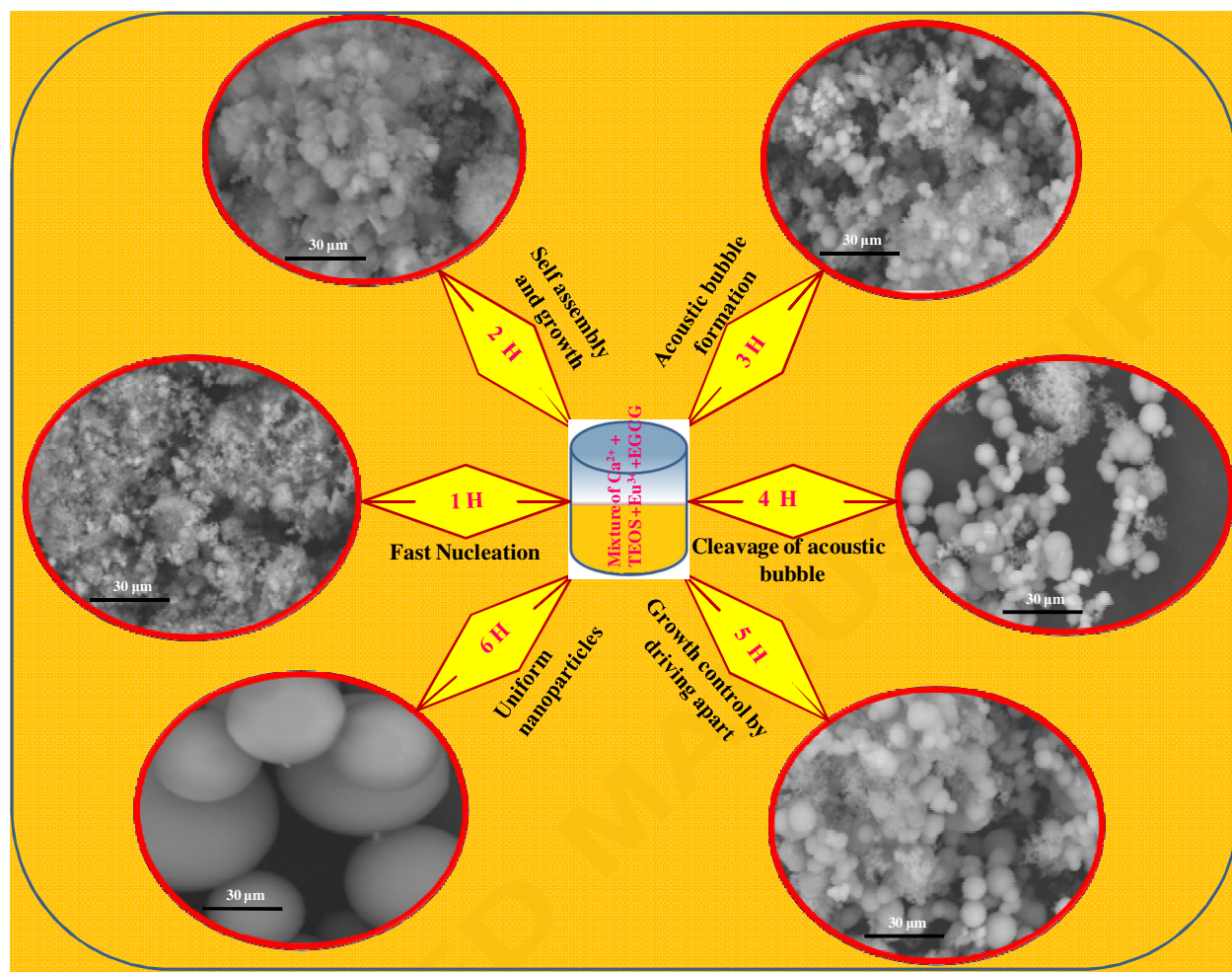


Fig.4. SEM images of $\text{Ca}_2\text{SiO}_4: \text{Eu}^{3+}$ (4 mol %) nanophosphor with different sonication times (1, 2, 3, 4, 5 and 6 h) with EGCG (25 ml).

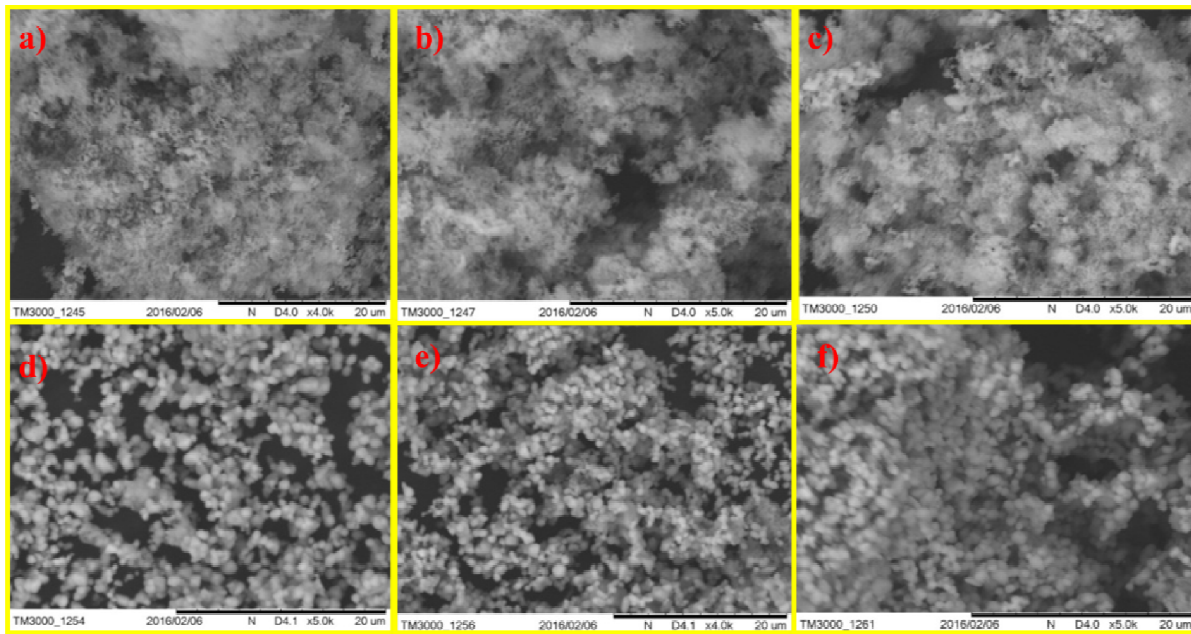


Fig.5. SEM images of $\text{Ca}_2\text{SiO}_4:\text{Eu}^{3+}$ (4 mol %) nanophosphor with different concentration of EGCG (10, 15, 20, 25, 30 and 35 ml) with 1hr of ultrasonic irradiation time.

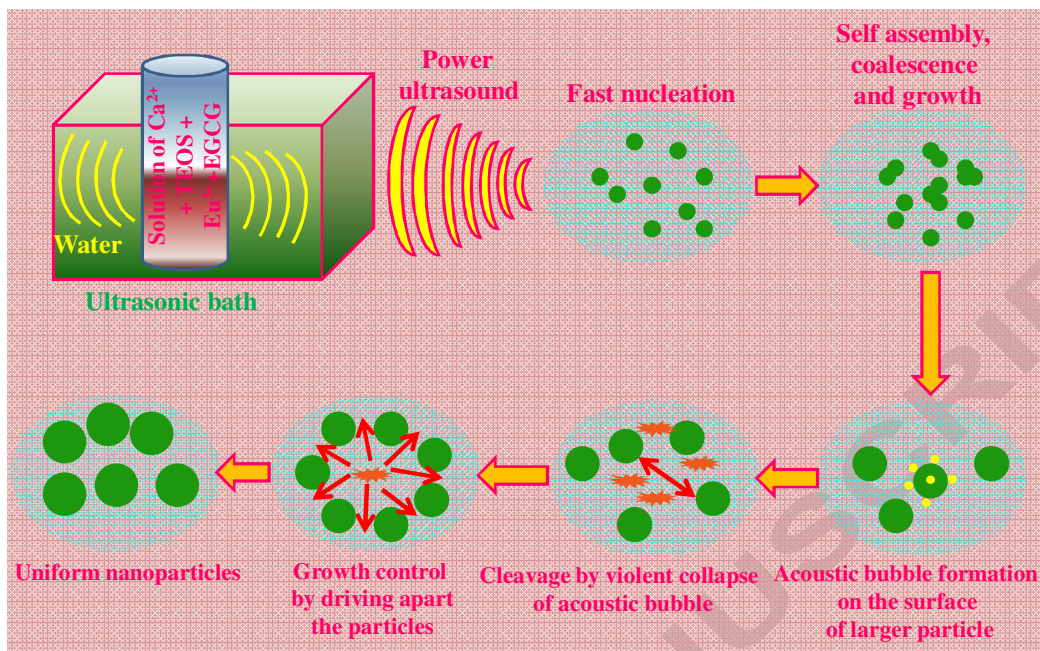


Fig.6.Schematic representation of formation process of hollow spheres morphology in $\text{Ca}_2\text{SiO}_4:\text{Eu}^{3+}$ (4 mol %) nanophosphor.

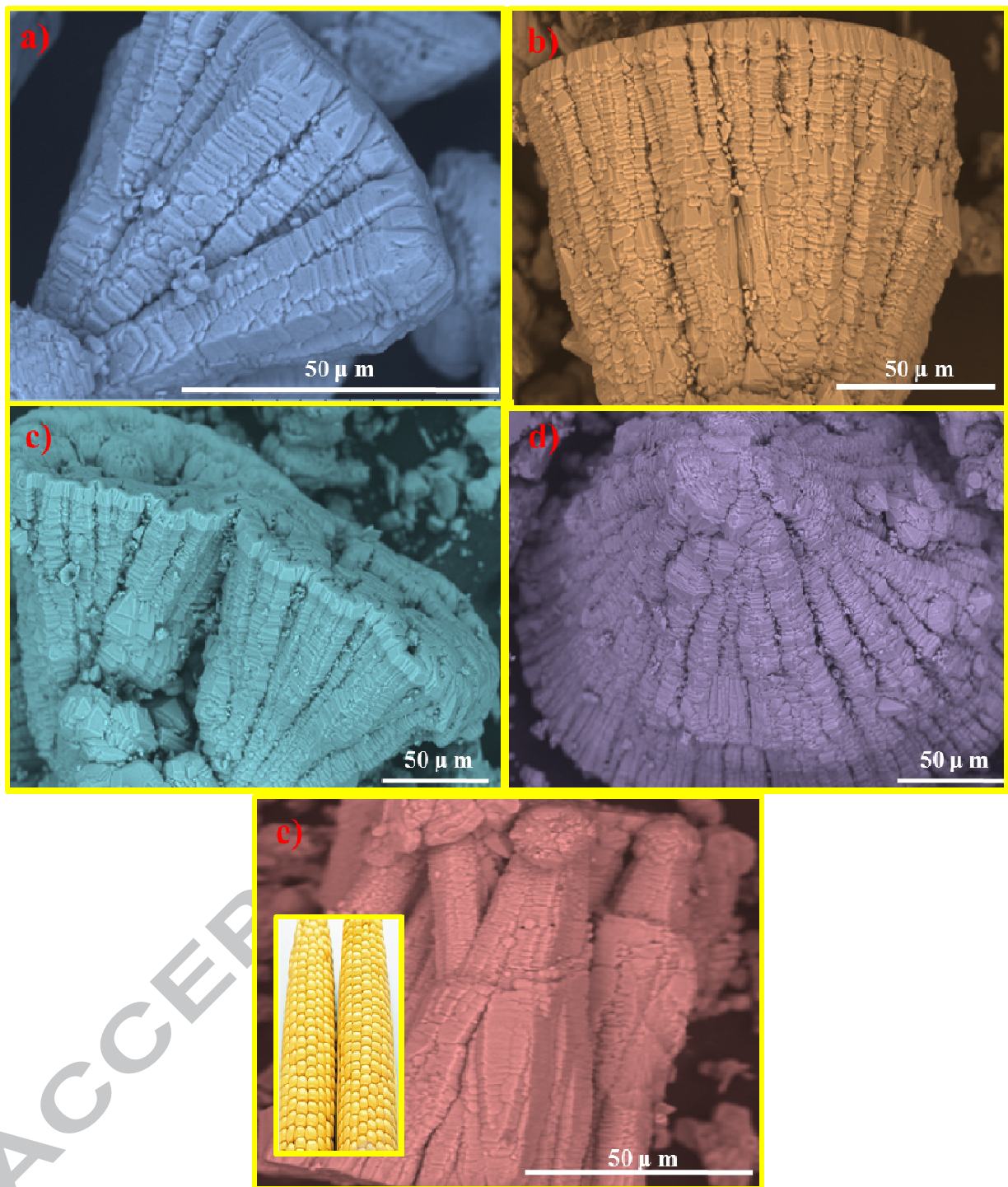


Fig.7(a). SEM images of $\text{Ca}_2\text{SiO}_4: \text{Eu}^{3+}$ (4 mol %) nanophosphor with various pH values (5, 7, 9, 11 and 12) with 1hr of ultrasonic irradiation time.

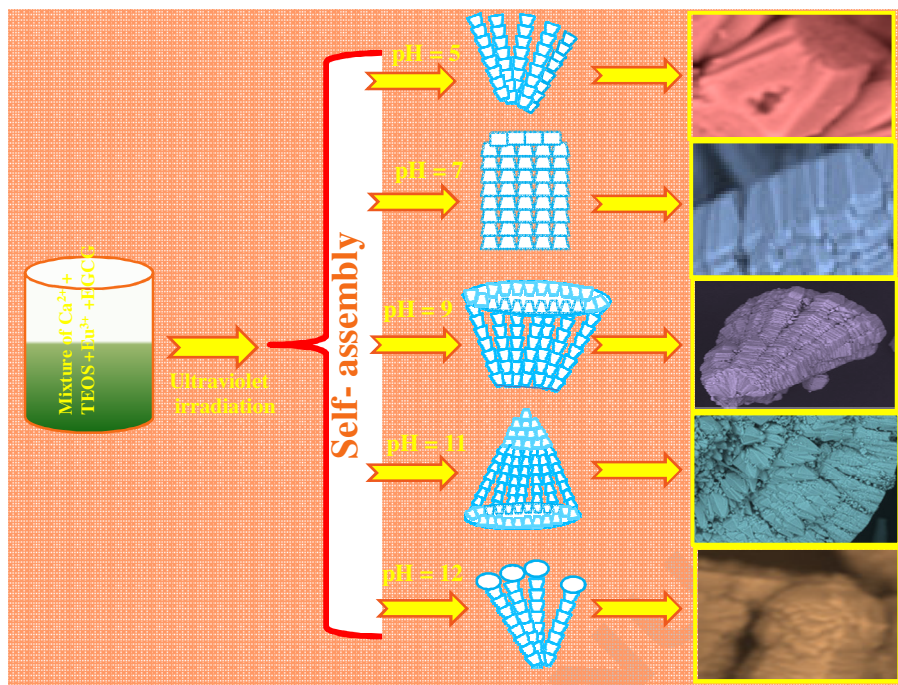


Fig.7 (b).Schematic representation for the formation of hierarchical superstructures of $\text{Ca}_2\text{SiO}_4:\text{Eu}^{3+}$ (4 mol %) nanophosphor with various pH values.

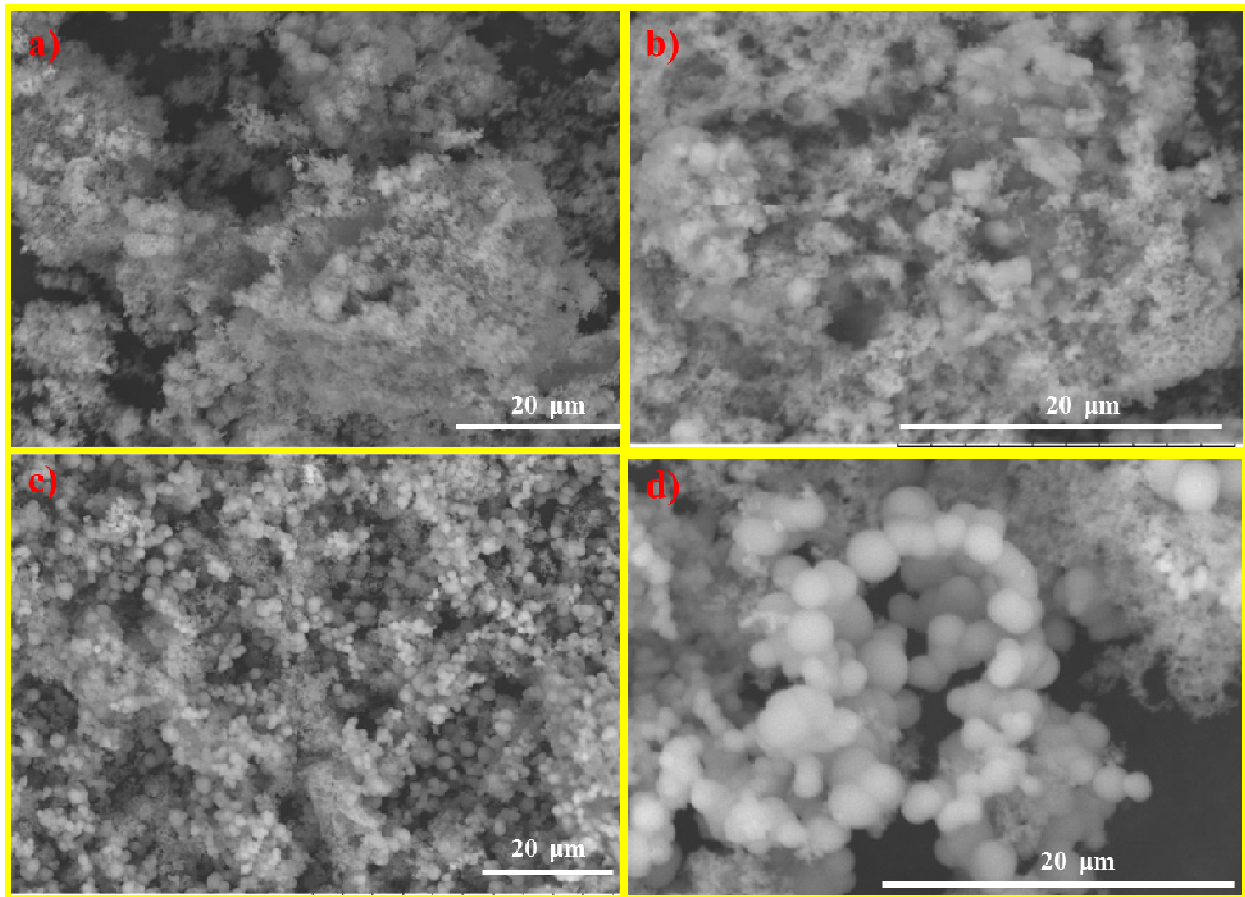


Fig.8. SEM images of Ca₂SiO₄: Eu³⁺ (4 mol %) nanophosphor with different sonication power (20 and 22 kHz).

ACCEPTED

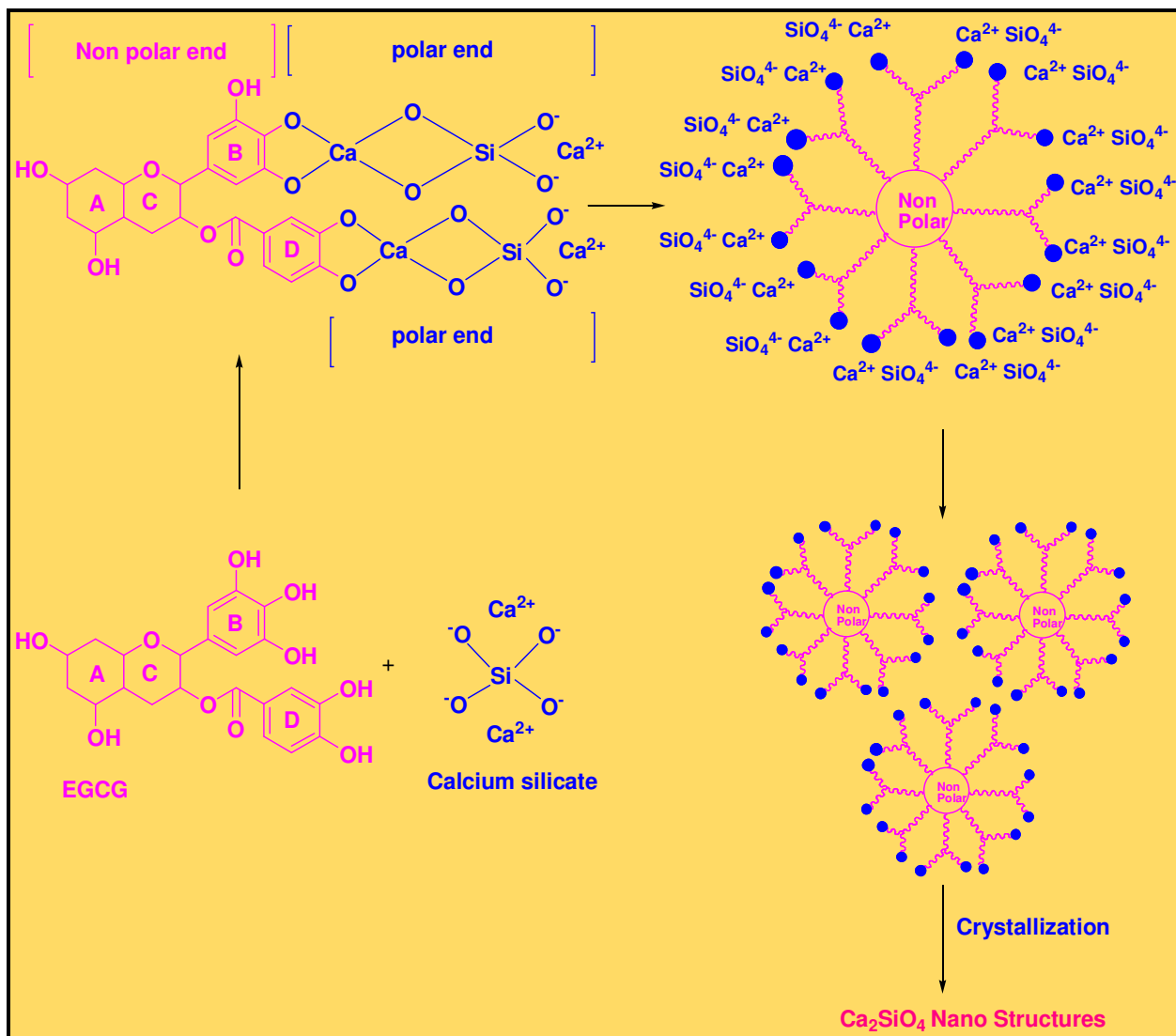


Fig.9. Schematic representation of $\text{Ca}_2\text{SiO}_4:\text{Eu}^{3+}$ nanostructures in the presence of EGCG.

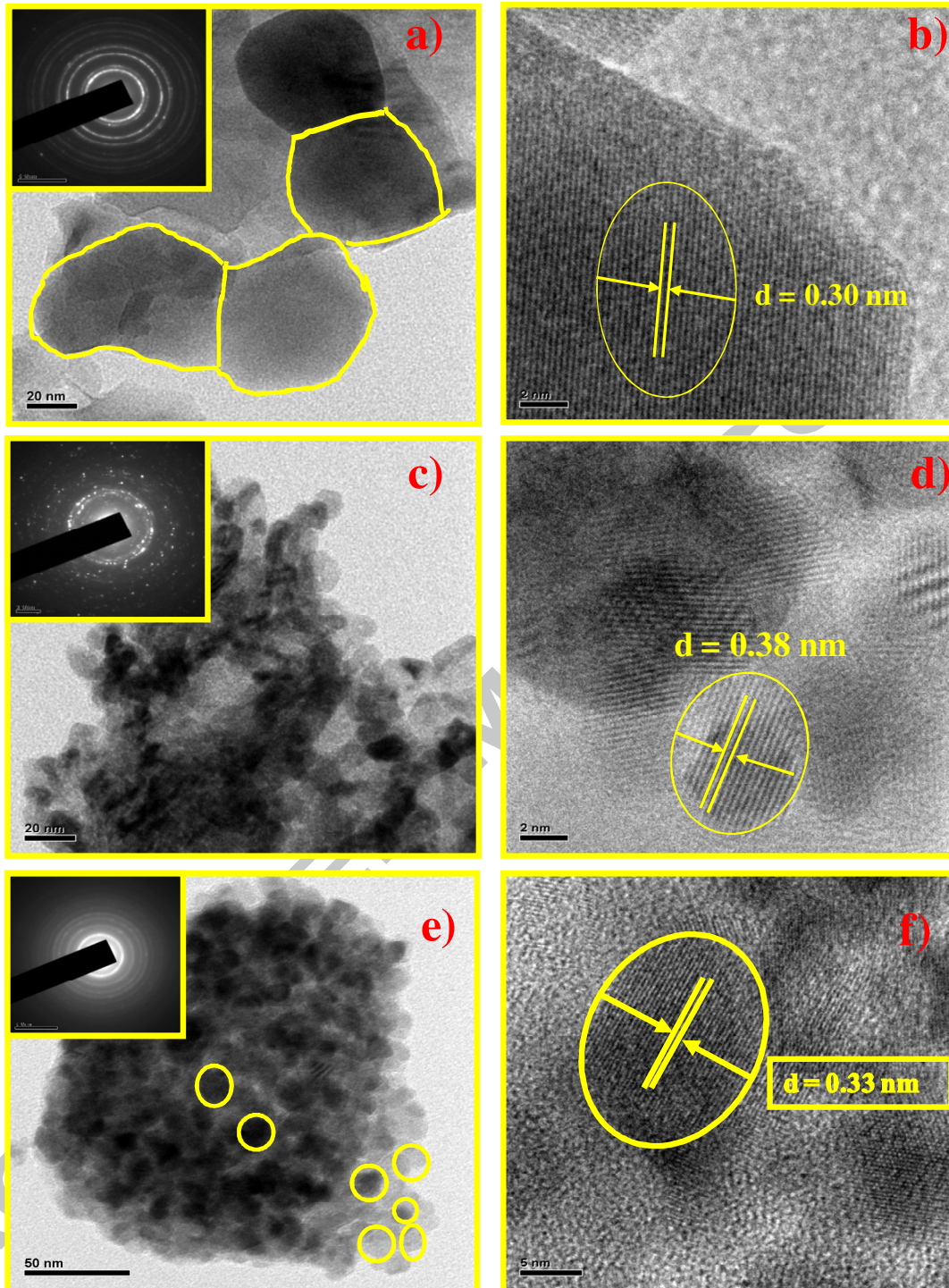


Fig.10. TEM and HRTEM images of $\text{Ca}_2\text{SiO}_4: \text{Eu}^{3+}$ (4 mol %) nanophosphor.

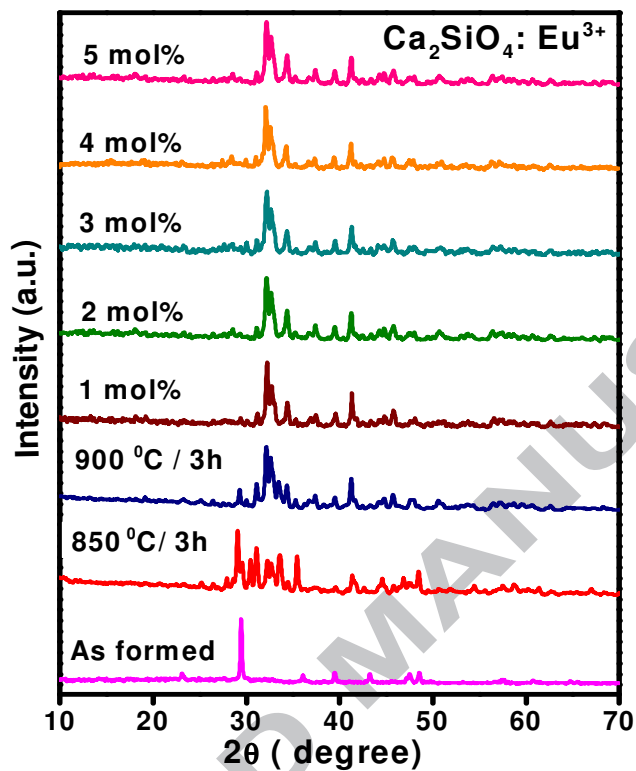


Fig.11. PXRD patterns of as formed and $\text{Ca}_2\text{SiO}_4:\text{Eu}^{3+}$ (1–5 mol %) nanophosphor.

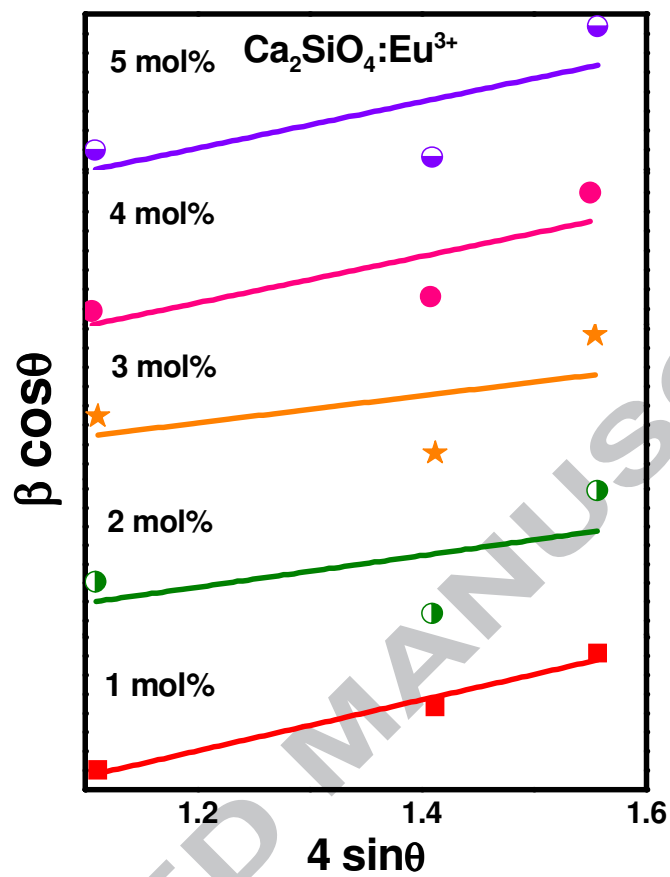


Fig.12. W-H plots of $\text{Ca}_2\text{SiO}_4:\text{Eu}^{3+}$ (1–5 mol %) nanophosphor.

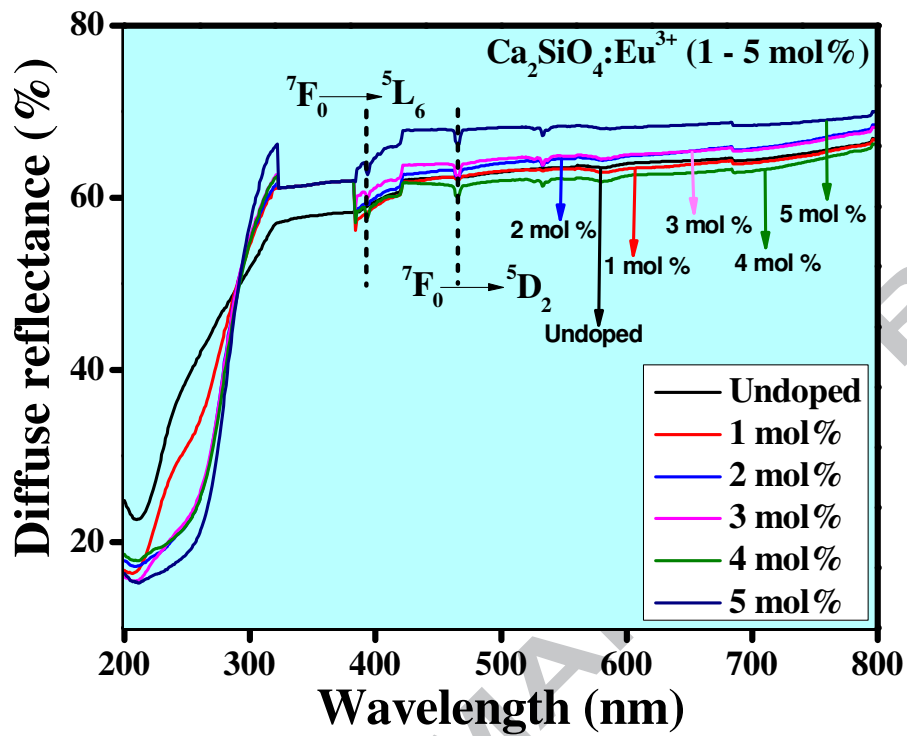


Fig.13. Diffuse reflectance spectra of undoped and $\text{Ca}_2\text{SiO}_4:\text{Eu}^{3+}$ (1–5 mol %) nanophosphor.

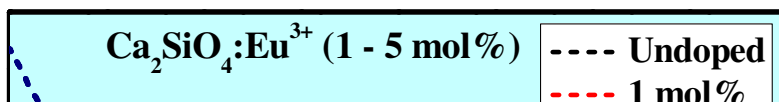


Fig.14. Energy band gaps of undoped and $\text{Ca}_2\text{SiO}_4:\text{Eu}^{3+}$ (1–5 mol %) nanophosphor.

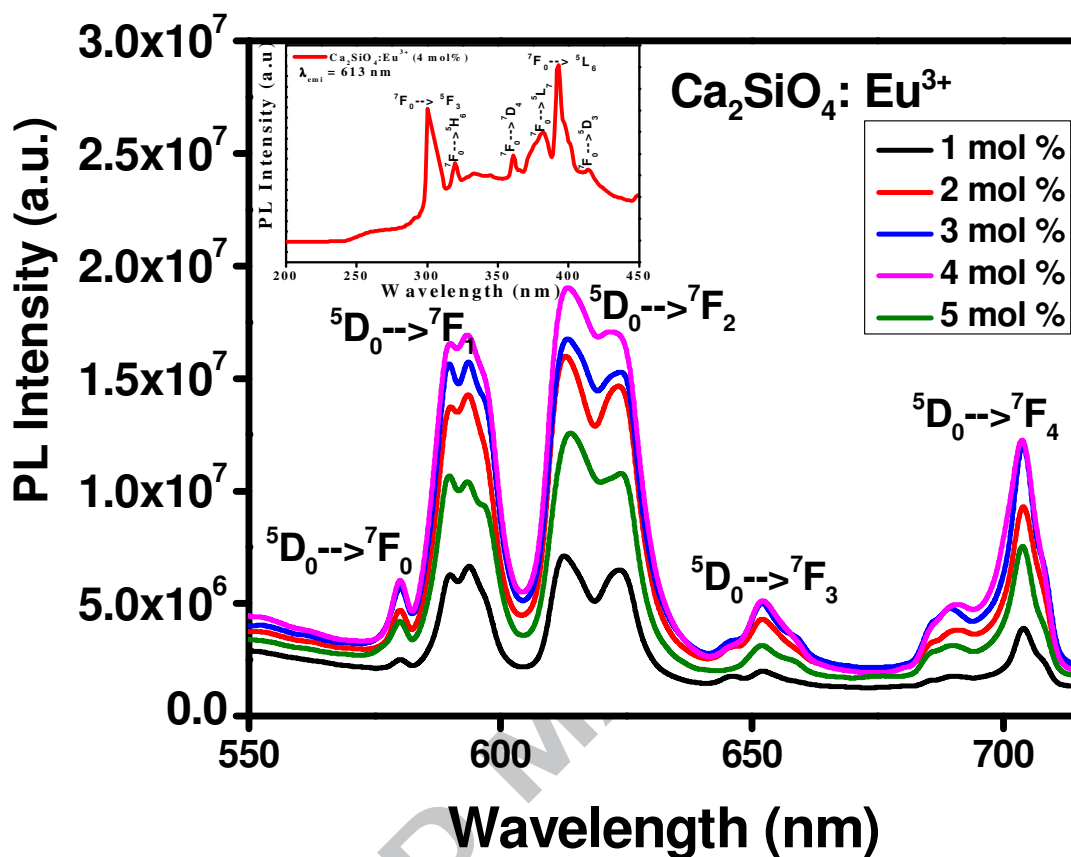


Fig.15. PL emission spectra of Ca₂SiO₄: Eu³⁺ (1–5 mol %) nanophosphor at $\lambda_{\text{exc}} = 393 \text{ nm}$. Inset shows the PL excitation spectra of Ca₂SiO₄: Eu³⁺ (4 mol%) nanophosphor at $\lambda_{\text{emi}} = 613 \text{ nm}$.

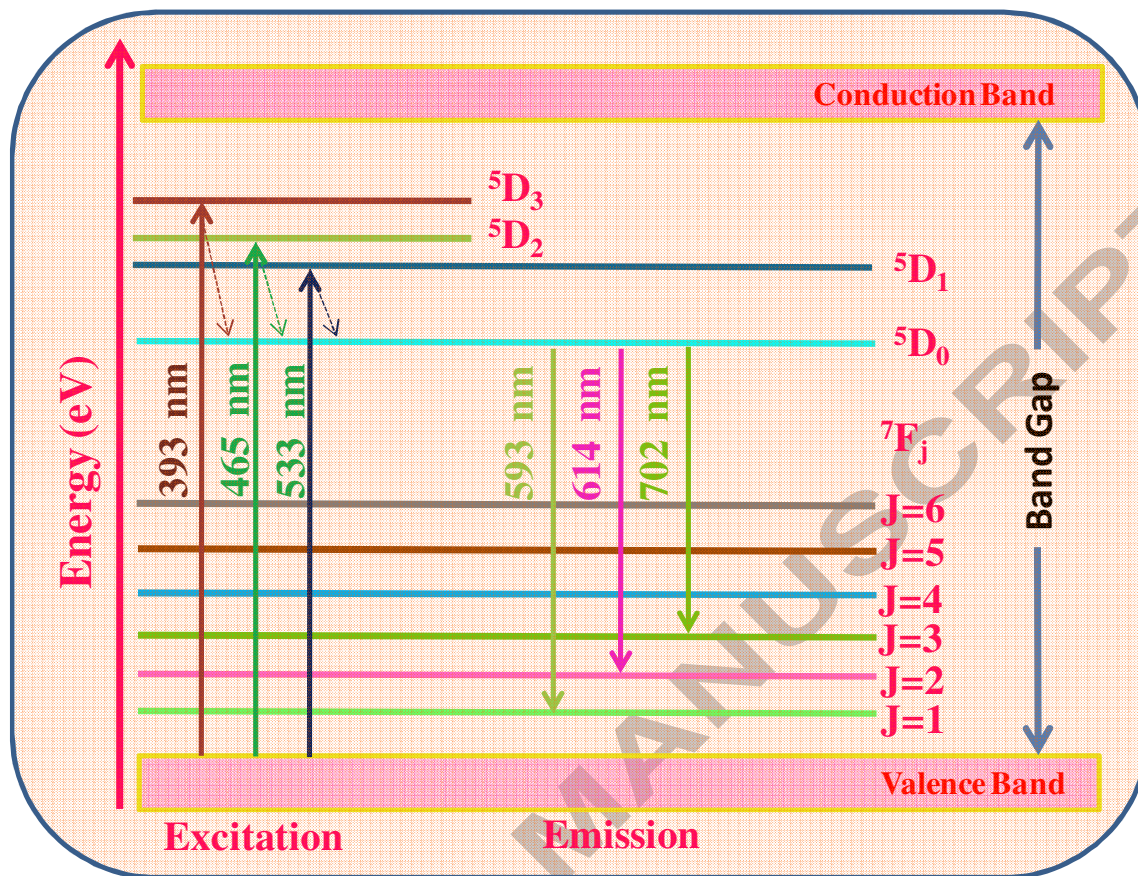


Fig.16. Energy levels diagram of Eu^{3+} doped Ca_2SiO_4 nanophosphor.

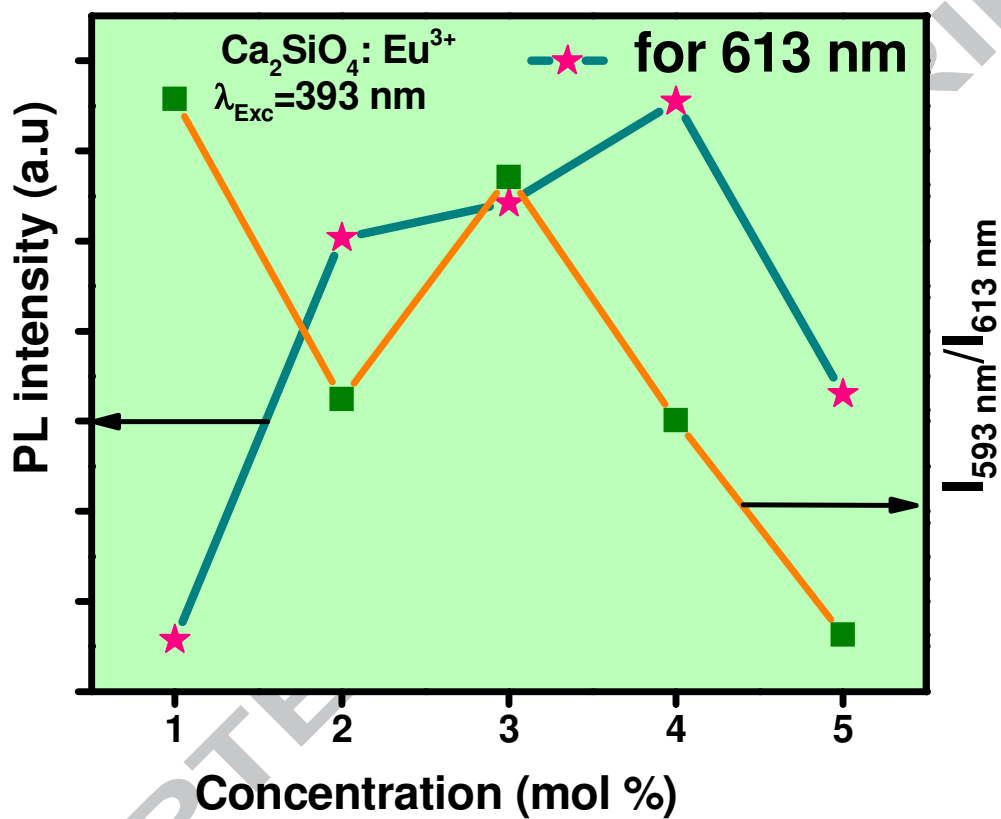


Fig.17. Effect of concentration of Eu^{3+} on the 614 nm emission and the variation of asymmetric ratio in Ca_2SiO_4 nanophosphors.

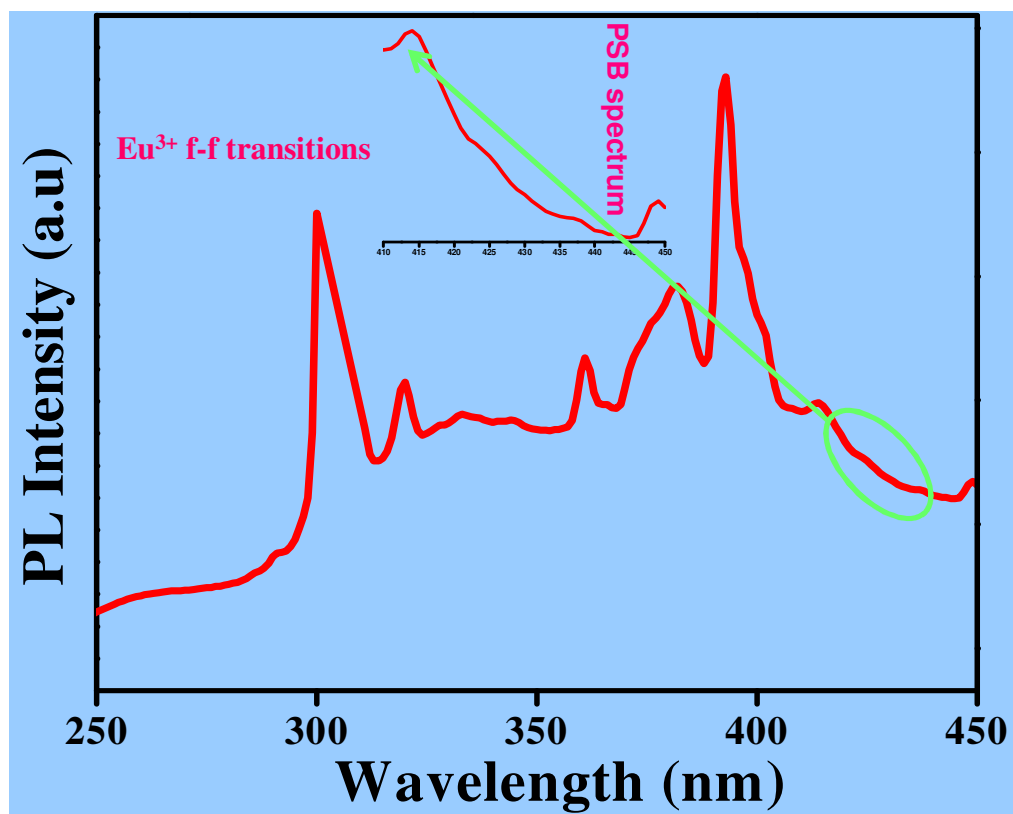


Fig.18. PL excitation spectrum, with the enlarge portion, showing the phonon assisted transition.

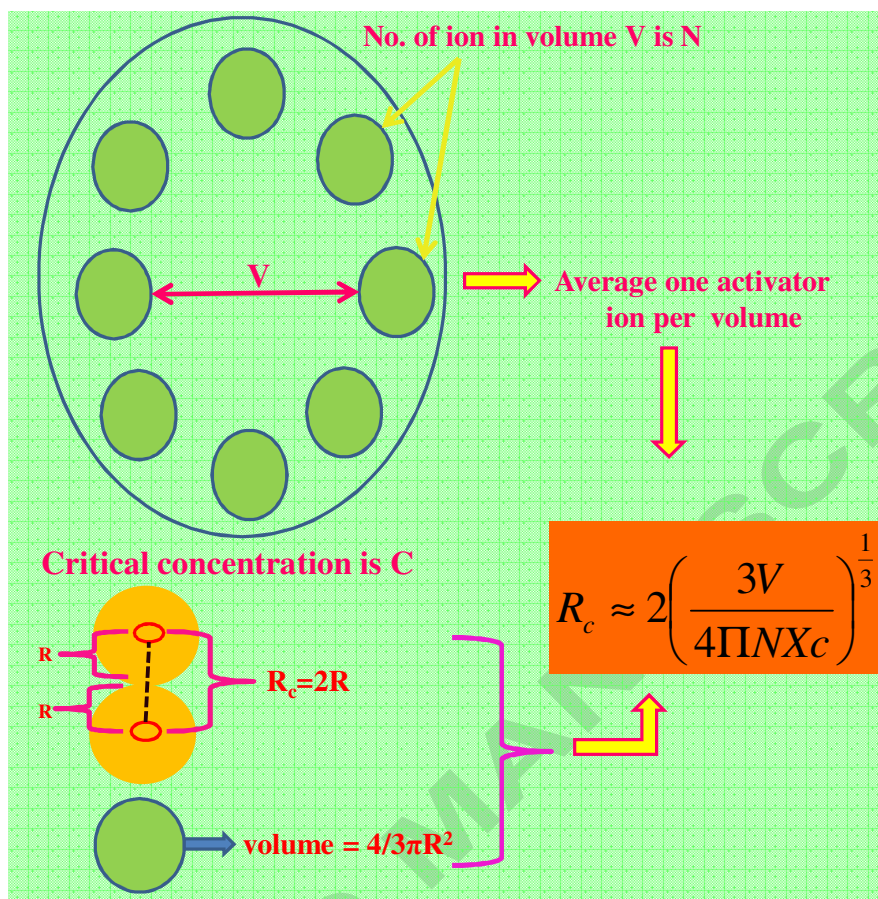


Fig.19. The schematic representation of Blasse's relation.

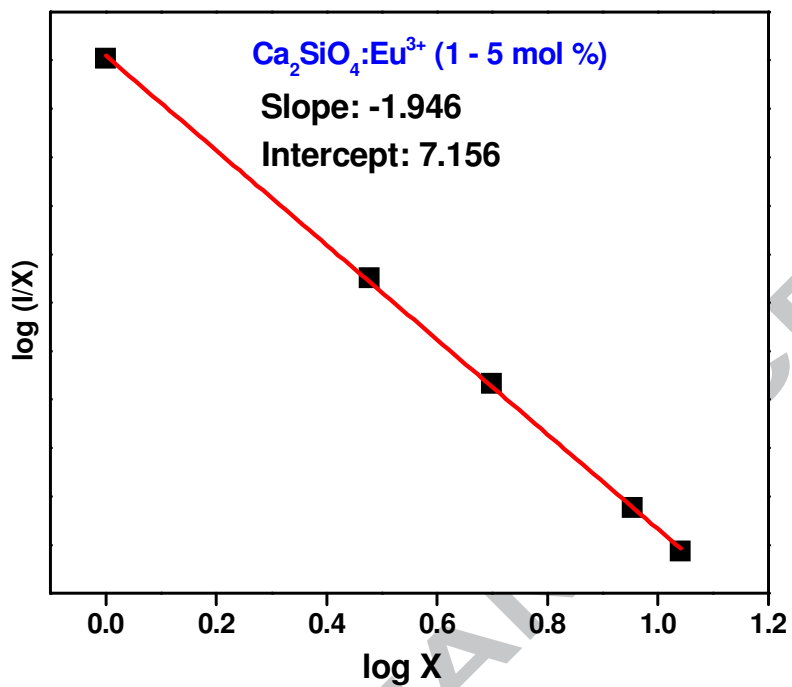


Fig. 20. Relation between $\log(x)$ and $\log(I/x)$ in $\text{Ca}_2\text{SiO}_4:\text{Eu}^{3+}$ (1–5 mol %) nanophosphor.

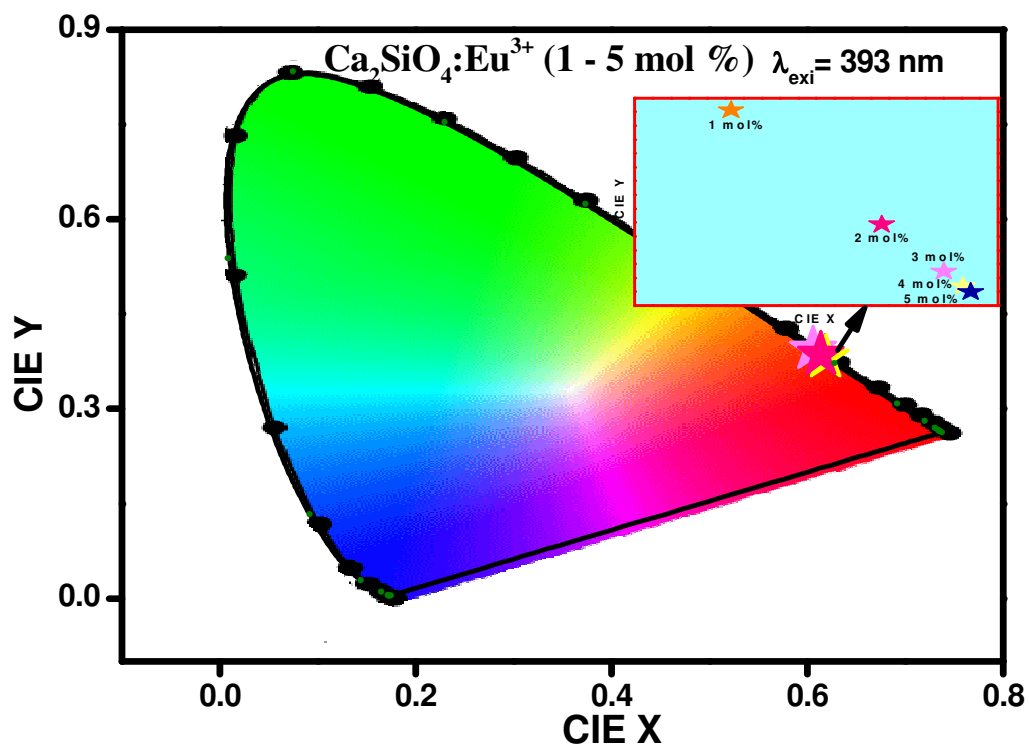


Fig.21. CIE diagram of $\text{Ca}_2\text{SiO}_4:\text{Eu}^{3+}$ (1-5 mol %) nanophosphor.

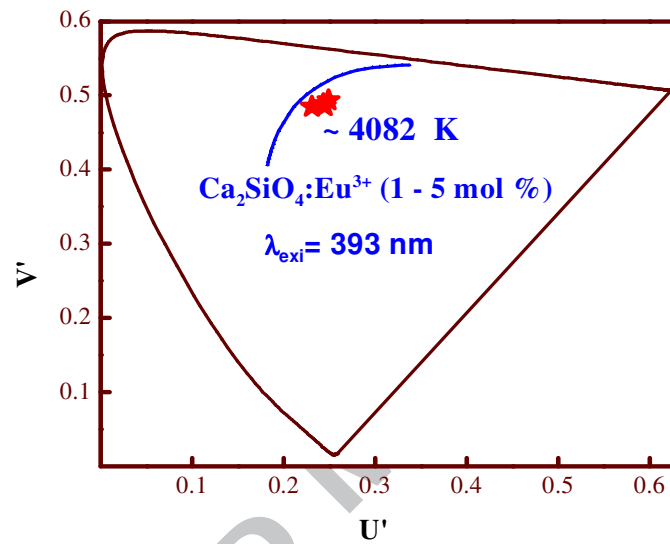


Fig.22. CCT diagram of $\text{Ca}_2\text{SiO}_4:\text{Eu}^{3+}$ (1-5 mol %) nanophosphor.

Table.1. Method of preparation, formation temperature and morphology of the product obtained in various silicate phosphors.

Material	Method of preparation	Formation temperature	Morphology of the product	Reference
$\text{Sr}_2\text{SiO}_4:\text{Eu}^{3+}$	Spray-drying process	1150 °C	Microspheres	Hao Feng et al. [10]
$\text{Sr}_2\text{SiO}_4:\text{Eu}^{3+}$	Solution combustion method	900 °C	Porous and irregular shaped particles	Nagabhushana et al. [11]
$\text{CaSrSiO}_4:\text{Eu}^{3+}$	Co-precipitating solvo- thermal	1200 °C	Pop-corn like structure	Sakthivel Gandhi et al. [12]
$\text{Zn}_2\text{SiO}_4:\text{xEu}^{3+}$	Solid state method	800 °C	Irregular shaped particles	Nur Alia Sheh Omar et al. [13]
$\text{Ca}_2\text{SiO}_4:\text{Eu}^{3+}$	Solution combustion process	950 °C	Highly porous and agglomerated particles	Sunitha et al. [14]
$\text{Mg}_2\text{SiO}_4:\text{Eu}^{3+}$	Solution combustion process	350 °C	Highly porous and irregular morphology	Ramachandra Naik et al. [15]
$\text{Mg}_2\text{SiO}_4:\text{Eu}^{3+}$	Polyacrylamide gel method	900 °C	Irregular shaped particles	Tabrizi et al. [16]
$\text{Ca}_2\text{SiO}_4:\text{Eu}^{3+}$	Sonochemical synthesis	900 °C	Hierarchical superstructures	Present work

Table.2. Chemicals used in the present study.

Material	Assay
Tetra ethyl orthosilicate	99.9% Sigma Aldrich (India)
Calcium nitrate	99.9% Sigma Aldrich (India)
Europium nitrate	99.9% Sigma Aldrich (India)
Anhydrous Sodium hydroxide	99% S D fine-chem. limited (India)
Ethanol	99% S D fine-chem. limited (India)
EGCG	99.9% Phyto Biotech Pvt. Ltd. (India)

Table 3: Estimated crystallite size, strain and energy gap (E_g) values of $\text{Ca}_2\text{SiO}_4:\text{Eu}^{3+}$ (1-5 mol %) nanophosphor.

Eu^{3+} conc. (mol %)	Crystallite size(nm) [D-S approach]	Crystallite		Strain ($\times 10^{-4}$)	E_g value
		size(nm)	size(nm)		
			[W-H approach]		
1	20.0	21	1.4	5.16	
2	20.5	23	1.7	4.82	
3	17.0	20	1.8	4.78	
4	20.6	24	1.4	4.75	
5	18.8	19	1.9	4.69	

Table.4. Photometric characteristics of Eu³⁺ doped Ca₂SiO₄ nanophosphors.

Eu³⁺ Concentration (mol %)	X	Y	CP (%)	CCT (K)
1	0.6053	0.3941	96.78	5860
2	0.6180	0.3814	94.28	3557
3	0.6170	0.3824	94.54	3293
4	0.6185	0.3810	95.78	3570
5	0.613	0.3858	96.63	4126

Table 5: Judd-Ofelt intensity parameters (Ω_2 , Ω_4), Emission peak wavelengths (λ_p in nm), radiative transition probability (A_T), calculated radiative (τ_{rad}) lifetime, branching ratio (β_R) and asymmetric ratio (A_{21}) of $\text{Ca}_2\text{SiO}_4:\text{Eu}^{3+}$ (1-5 mol %) compounds ($\lambda_{ex} = 393$ nm).

$\text{Ca}_2\text{SiO}_4:\text{Eu}^{3+}$ conc. (mol%)	Judd-Ofelt intensity parameters ($\times 10^{-20} \text{ cm}^2$)		Emission peak wavelength λ_p in nm	A_T (s^{-1})	τ_{rad} (ms)	β_R	A_{21}
	Ω_2	Ω_4					
1	3.66	5.01	613.14	82.51	12.11	0.999	0.945
2	3.87	5.56	612.80	87.19	11.46	0.998	0.891
3	3.72	6.58	613.32	83.84	11.92	0.993	0.931
4	3.89	6.13	612.80	87.56	11.42	0.999	0.888
5	4.11	6.06	613.74	92.70	10.78	0.998	0.849

Research highlights

1. $\text{Ca}_2\text{SiO}_4:\text{Eu}^{3+}$ hierarchical superstructures were synthesized by facile EGCG ultrasound assisted synthesis.
2. The particle nucleation and growth of $\text{Ca}_2\text{SiO}_4:\text{Eu}^{3+}$ superstructures were analyzed systematically.
3. Plausible mechanisms for the morphological evolution of superstructures were proposed.
4. The obtained superstructures could be a promising red component for possible applications in white LEDs.

ACCEPTED MANUSCRIPT